J. Fluid Mech. (2025), *vol.* 1007, A43, doi:10.1017/jfm.2025.79

JFM PAPERS

Locomotion of paired spermatozoa during flagellar synchronisation

Kaixuan Zhang[1], **Aaron Lewis**[2], **Anke Klingner**[3], **Veronika Magdanz**[2], **Sarthak Misra**[1,4] and **Islam S.M. Khalil**[5]

[1]Department of Biomaterials and Biomedical Technology, University Medical Center Groningen, University of Groningen, Groningen 9713 AV, Netherlands

[2]Department of Systems Design Engineering, University of Waterloo, Waterloo N2L 3G1, Canada

[3]Department of Physics, The German University in Cairo, New Cairo 11835, Egypt

[4]Department of Biomechanical Engineering, University of Twente, Enschede 7522 NB, Netherlands

[5]RAM-Robotics and Mechatronics, University of Twente, Enschede 7522 NB, Netherlands

Corresponding authors: Kaixuan Zhang, k.zhang@umcg.nl; Islam S.M. Khalil, i.s.m.khalil@utwente.nl

(Received 30 May 2024; revised 15 October 2024; accepted 12 January 2025)

Microorganisms, such as spermatozoa, exhibit rich behaviours when in close proximity to each other. However, their locomotion is not fully understood when coupled mechanically and hydrodynamically. In this study, we develop hydrodynamic models to investigate the locomotion of paired spermatozoa, predicting the fine structure of their swimming. Experimentally, sperm pairs are observed to transition between different modes of flagellar synchronisation: in-phase, anti-phase and lagged synchronisation. Using our models, we assess their swimming performances in these synchronisation modes in terms of average swimming speed, average power consumption, and swimming efficiency. The swimming performances of paired spermatozoa are shown to depend on their flagellar phase lag, flagellar waveforms, and the mechanical coupling between their heads.

Key words: micro-organism dynamics, propulsion

1. Introduction

Flagella or cilia are ubiquitous organelles in eukaryotic cells. They play a crucial role in physiological processes in animals, such as cerebrospinal fluid flow (Olstad *et al.* 2019), maintenance of the circadian clock (Tu *et al.* 2023), and mucociliary clearance in the respiratory system (Nawroth *et al.* 2019). In the microscopic world, unicellular organisms use their flagella/cilia to efficiently forage and travel, employing diverse locomotion strategies (Tam & Hosoi 2011; Omori *et al.* 2020). For instance, *Paramecium* is known to regulate its ciliary beating to swim forwards, swim backwards and reorient (Machemer & Eckert 1973; Okamoto & Nakaoka 1994; Ishikawa & Hota 2006). *Escherichia coli* exhibits a run-and-tumble locomotion by bundling and unbundling its flagella (Berg & Brown 1972). The biflagellate alga *Chlamydomonas* transitions between two swimming gaits by modulating the synchronisation of its two flagella (Polin *et al.* 2009). Spermatozoa, however, adopt a distinct locomotion strategy by assembling into bundles with their heads attached. This cooperative behaviour has been found to increase their swimming speed (Woolley *et al.* 2009; Fisher & Hoekstra 2010), providing potential advantages in sperm competition (Moore *et al.* 2002; Immler 2008).

The increased velocity along the average path of sperm bundles during one beat cycle has been attributed to either their straighter swimming trajectory (Fisher *et al.* 2014; Pearce *et al.* 2018) or their synchronised flagellar beating when the difference between the flagellar beating phase $\Delta\phi$ is a constant for beat cycles (Woolley *et al.* 2009; Zhang *et al.* 2023). While it has been observed experimentally that in-phase flagellar synchronisation ($\Delta\phi = 0$) can increase the swimming speed of paired sperm cells (Woolley *et al.* 2009; Zhang *et al.* 2023), the computational investigation indicates that increased speed results only from anti-phase flagellar synchronisation ($\Delta\phi = \pi$) or large flagellar phase lags ($\Delta\phi > \pi/4$) (Cripe *et al.* 2016). This discrepancy highlights the complexity of the collective dynamics of sperm bundles. Rich behaviours are also discovered in a simple system comprising two adjacent but separate microswimmers, e.g. hydrodynamic attraction/repulsion (Yang *et al.* 2008; Carichino *et al.* 2021), alignment (Olson & Fauci 2015; Taketoshi *et al.* 2020), oscillation (Pooley *et al.* 2007; Carichino *et al.* 2021) and synchronisation (Di Leonardo *et al.* 2012; Tătulea-Codrean & Lauga 2022; Samatas & Lintuvuori 2023). These behaviours depend on their waveforms and relative displacement, phase and orientation (Pooley *et al.* 2007; Elfring & Lauga 2011*a*). Furthermore, current models infer that the hydrodynamic synchronisation of co-swimming cells requires geometrically asymmetric waveforms or the presence of a viscoelastic fluid environment (Elfring & Lauga 2009, 2011*b*; Elfring *et al.* 2010). Their swimming speed and efficiency would increase drastically if co-swimming cells mechanically adhere into pairs (Simons & Rosenberger 2021). These factors also contribute to the rich dynamics observed in other microbial and artificial swimming systems (Drescher *et al.* 2011; Elgeti *et al.* 2015; Pramanik *et al.* 2024).

Despite many studies on the system of multiple separate microorganisms, the influence of flagellar beating on the locomotion of paired spermatozoa remains largely unexplored experimentally. A few challenges may account for the insufficiency of investigation. First, only a tiny proportion of sperm cells form pairs, restricting the sample size for experimental observation. Second, sperm locomotion is influenced by complex mechanical and hydrodynamic cell–cell and cell–environment interactions, which depend on their flagellar beat patterns and external factors, e.g. the geometry of surrounding environments (Raveshi *et al.* 2021), fluid viscoelasticity (Tung *et al.* 2017; Zaferani *et al.* 2021) and chemoattractants (Friedrich & Jülicher 2007; Li *et al.* 2023; Zaferani & Abbaspourrad 2023). As a result, it is difficult to control the flagellar beat pattern and experimentally investigate its influence on the locomotion of sperm pairs. Experimental studies of paired spermatozoa have been limited to comparing out-of-phase and in-phase flagellar beat patterns due to these challenges (Woolley *et al.* 2009; Zhang *et al.* 2023).

In our experiments, bovine sperm pairs of two cells with their heads attached were observed in a chamber with a half-depth $h = 10\ \mu\text{m}$ (figure 1*a*). They swam in a plane parallel to the boundary surface of the chamber with primarily planar flagellar beats, similar to the previous experimental observations (Winet *et al.* 1984; Woolley 2003;

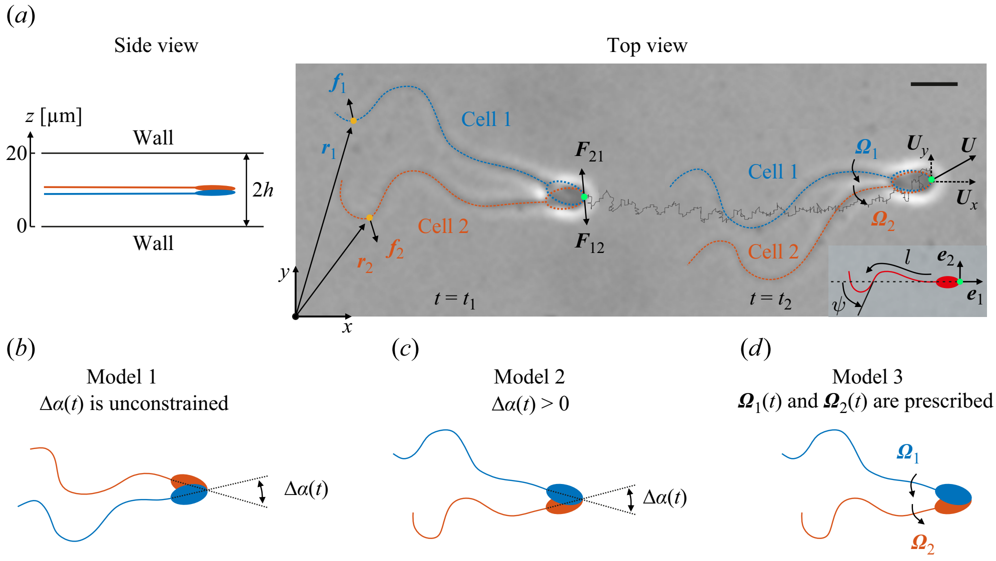

Figure 1. (a) Schematic of a pair of bovine spermatozoa swimming in a 20 μm deep chamber with their heads attached. The paired sperm cells at two instants are overlaid at the same frame of reference. Any point on the ith cell can be described by the position vector $\boldsymbol{r}_i$ with respect to the laboratory frame. The ith cell experiences a hydrodynamic force $\boldsymbol{f}_i$ at an arbitrary point $\boldsymbol{r}_i$. The heads of the sperm pair are attached, with no relative translational motion allowed. But they can oscillate relatively about the pivot point (head tip) with instantaneous angular velocities $\boldsymbol{\varOmega}_i$, $i = 1, 2$. The instantaneous translational velocity of the sperm pair $\boldsymbol{U}$ is represented by that of the pivot point. Inset: the comoving frame is spanned by the orthonormal unit vectors $\boldsymbol{e}_1$ and $\boldsymbol{e}_2$, and its origin overlaps with the pivot point. The flagellar shape in the comoving frame can be described by the local tangent angle ψ. Forces F_{ij} exist between the ith head and the jth head, and are specified differently based on the simplification of the head–head attachment. Three models are developed to investigate the locomotion of paired spermatozoa. (*b*) In model 1, the head orientation difference $\Delta\alpha$ is unconstrained, such that $\Delta\alpha$ can be positive, zero or negative. (*c*) In model 2, $\Delta\alpha$ is constrained such that $\Delta\alpha > 0$. (*d*) Time-varying head angular velocities $\boldsymbol{\varOmega}_i$, $i = 1, 2$, are extracted from experiments and prescribed in model 3. Scale bar: 10 μm.

Woolley *et al.* 2009). The paired sperm cells were experimentally observed to transition between different modes of flagellar synchronisation: in-phase ($\Delta\phi = 0$), anti-phase ($\Delta\phi = \pi$) and lagged synchronisation ($\Delta\phi$ is a constant not equal to 0 or π). To investigate the influence of flagellar phase lag $\Delta\phi$ on the swimming of sperm pairs, we develop a three-dimensional hydrodynamic model, referred to as model 1. The attachment between the heads involves adhesion proteins on the head surface and is influenced by factors such as cyclic adenosine monophosphate (cAMP) and sperm antagglutin on the head surface (Lindahl & Sjöblom 1981; Flaherty *et al.* 1993). Considering the as yet not fully understood mechanical coupling due to the head–head attachment, in model 1, we simplify the mechanical head–head coupling as an adhesive force $\boldsymbol{F}^{\mathrm{a}}_{ij}$ between the ith head and jth head. In model 1, the relative oscillation between the heads in a sperm pair is not constrained, such that their orientation difference $\Delta\alpha = \alpha_2 - \alpha_1$ can be positive, zero or negative (figure 1*b*). In addition, we experimentally observed that the relative oscillation between the heads of paired sperm cells started and paused seemingly randomly, consistent with previous experimental observations (Woolley *et al.* 2009; Zhang *et al.* Zhang *et al.* 2023). Their orientation difference $\Delta\alpha$ was always a positive value during swimming. Based on these experimental observations, we speculate that a steric force $\boldsymbol{F}^{\mathrm{s}}_{ij}$ may exist between the heads, besides the adhesive force. Therefore, based on model 1, we develop a second model, referred to as model 2, to explore this potential case where both adhesive and steric forces exist between the sperm heads. In model 2, the relative oscillation between the heads is constrained, such that their orientation difference is $\Delta\alpha > 0$ during the whole course of swimming (figure 1*c*). Both models 1 and 2 are used to investigate the phase-lag dependence of the swimming performances of paired spermatozoa regarding three parameters: average swimming speed, average power consumption, and swimming efficiency. For each specific flagellar phase lag $\Delta\phi$, its value is prescribed and fixed during the simulation. In models 1 and 2, the head angular velocities $\boldsymbol{\Omega}_i(t)$ $(i = 1, 2)$ are determined based on force-balance and torque-balance conditions for sperm cells at the low Reynolds number. To further explore the influence of head oscillation on the swimming trajectory of sperm pairs, a third model (referred to as model 3) is developed by providing model 1 with experimentally measured head angular velocities$\boldsymbol{\Omega}_i(t)$ $(i = 1, 2)$ (figure 1*d*). For more realistic representations, flagellar waveforms are reconstructed from our experimental measurements and prescribed in all our models.

2. Tracking of paired spermatozoa in a chamber

Cryopreserved bovine spermatozoa were obtained from Semex Inc (Guelph) and stored in liquid nitrogen. Semen straws were thawed in a 37 °C water bath for 2 min, before suspending the cells in 2 ml high glucose Dulbecco's Modified Eagle's Medium (DMEM, D6546 Sigma Aldrich). Sperm cells were washed twice by centrifugation at 300 g for 5 min, and resuspended in a 2 ml clean medium. Then 0.3 % Methyl cellulose (M0512, Sigma Aldrich) was added to increase the viscosity of the medium. Five microlitres of sperm suspension were pipetted into slides with chamber depth 20 μm for immediate videomicroscopy.

Videomicroscopy was performed in an inverted Nikon microscope with a FastCam SA1.1 high-speed camera and a 40× objective in phase contrast mode, obtaining video sequences with 500 frames per second. In our experiments, paired spermatozoa with their heads attached were observed (see supplementary movie 1). We track the flagella using the customised script in Matlab. The algorithm detects first the head tip and then the junction between the head and flagellum, from which the orientation of each cell is derived. Subsequently, the flagellum of each cell is tracked using the method reported by Geyer *et al.* (2013) and Riedel-Kruse *et al.* (2007). The tracked images need to be examined manually, and modified when the detection sometimes fails, due to e.g. dirt particles and overlapped flagella. Along each flagellum, 45 points are tracked. These flagellum points are off to both sides of the flagellum's centreline and are not equally spaced. A Savitzky–Golay filter with degree 3 and a span of 5 sequential flagellum points is used to filter the flagellum points. These filtered flagellum points are then interpolated with splines. The arc length of the flagellum is determined by summing the lengths of the splines, and points at equal distances of 0.25 μm along the flagellum are then determined. These equidistant points along the ith flagellum of a sperm pair are time-varying and used to determine their velocity $\boldsymbol{v}_i$ relative to the ith head.

3. Characterisation of the locomotion of paired spermatozoa

Bovine spermatozoa are approximately 60 μm in length. Approximately 0.1−3 % of them, depending on conditions, formed bundles, most of which were sperm pairs (Morcillo i Soler *et al.* 2022). Considering their approximately planar kinematics, we can describe their projected locomotion on the two-dimensional plane where they swim, and neglect the out-of-plane component, as shown in figure 1. The ith sperm head of a sperm pair can be described by its orientation $\alpha_i(t)$ and the position of its head tip $\boldsymbol{r}_{\mathrm{p}}(t)$ with respect to the laboratory frame. The flagellar shape can be described by the tangent angle ψ with respect to the comoving frame spanned by the orthonormal unit vectors $\boldsymbol{e}_1$ and $\boldsymbol{e}_2$. Here, $\boldsymbol{e}_1$ and $\boldsymbol{e}_2$ are oriented along the long and short axes of the projection of the ellipsoidal head on the swimming plane, respectively, as illustrated in figure 1 (inset). The tangent angle $\psi(l, t),\ 0 \le l \le 2L$, is enclosed between $\boldsymbol{e}_1$ and the local tangent vector to the flagellar centreline, where L is the half-length of the flagellum. The flagellar shape with respect to the laboratory frame at a time t can be characterised by

$$\boldsymbol{r}_{\mathrm{f}}(l, t) = \boldsymbol{r}_{\mathrm{p}}(t) - a\boldsymbol{e}_1 - \int_0^l \mathrm{d}l' \left[\cos\psi(l', t)\, \boldsymbol{e}_1 + \sin\psi(l', t)\, \boldsymbol{e}_2\right], \tag{3.1}$$

where a is the major axis of the projection of the head on the swimming plane (Friedrich *et al.* 2010). Here, $\boldsymbol{r}_{\mathrm{f}}(0, t)$ corresponds to the head–flagellum junction, and $\boldsymbol{r}_{\mathrm{f}}(2L, t)$ corresponds to the distal end of the flagellum. This description can be applied to the two flagella of a sperm pair. Any point on the ith cell with respect to the laboratory frame is represented by $\boldsymbol{r}_i(s, t)$, where s is the coordinate of this point.

4. Mechanical and hydrodynamic cell–cell interactions

In our experiments, paired bovine sperm cells, one head on top of the other, oscillated their heads during swimming. From the top view, a portion of the heads, e.g. the head tips, remained overlapping during the whole course of swimming (figure 1). The head tips were the pivot point about which the heads oscillated. The attachment between the heads allowed their relative oscillation within the swimming plane, but constrained their relative translational motion. Similar experimental observations have been reported previously (Woolley *et al.* 2009; Zhang *et al.* 2023). The head of a bovine spermatozoon resembles an approximately flattened ellipsoid, with detailed cellular morphologies (Pesch & Bergmann 2006; Carvalho *et al.* 2013). In our models, we ignore the detailed morphologies of the bovine sperm head and only consider its three principal dimensions – length, width and height. Thus the sperm head is simplified as an ellipsoid with dimensions $9 \times 5 \times 0.4\ \mu\mathrm{m}$ (length × width × height) in our models, based on previous experimental measurements (Pesch & Bergmann 2006; Carvalho *et al.* 2013). The flagellum is approximately a tube with half-length $L = 25\ \mu\mathrm{m}$ and radius $\rho = 0.25\ \mu\mathrm{m}$ (Pesch & Bergmann 2006; Carvalho *et al.* 2013). These dimensions for the flagellum are used in our models.

Previous computational studies have shown that the hydrodynamic interaction between two adjacent but separate flagella may lead them to swim away from each other in the three-dimensional space (Simons *et al.* 2015; Carichino *et al.* 2021). However, compared with hydrodynamic forces, the mechanical head–head coupling is strong, so that paired sperm cells continue to swim together (Woolley *et al.* 2009; Zhang *et al.* 2023). Therefore, the mechanical head–head coupling and its influence on the swimming of paired spermatozoa cannot be ignored. We simplify the as yet not fully understood head–head coupling as a pair of adhesive forces on the pivot point $\boldsymbol{F}_{ij}^{\mathrm{a}},\ i = 1, 2$, elaborated on in § 4.1. Here, the force on the ith head $\boldsymbol{F}_{ij}^{\mathrm{a}}$ results from the interaction with the jth head, such that $F_{12}^{\mathrm{a}} = -F_{21}^{\mathrm{a}}$. For the second potential case where both adhesive and steric forces exist between the heads, we develop model 2 based on model 1, detailed in § 4.2.

4.1. *Model of paired spermatozoa with adhesive forces between their heads*

Let $\boldsymbol{\Omega}_i(t),\ i = 1, 2$, denote the instantaneous angular velocity of the ith head about the pivot point, and let $\boldsymbol{U}(t)$ denote the instantaneous translational velocity of the pivot point, with respect to the laboratory frame. The velocity $\boldsymbol{v}_i(s, t)$ at an arbitrary point on the ith flagellum with respect to the comoving frame is obtained from our experimentally observed time-varying flagellar shapes. Given $\boldsymbol{v}_i(s,t)$, the velocity $\boldsymbol{u}_i(s,t)$ at this point in the laboratory frame is

$$\boldsymbol{u}_i(s,t) = \boldsymbol{v}_i(s,t) + \boldsymbol{U}(t) + \boldsymbol{\varOmega}_i(t) \times \boldsymbol{r}'_i(s,t), \tag{4.1}$$

where $\boldsymbol{r}'_i(s,t)$ is the position vector of this point in the comoving frame (Bayly *et al.* 2011). For the velocity of any point on the head, (4.1) is also applicable, where the first term on the right-hand side vanishes. The sperm cells are spatially discretised, as detailed in Appendix A. For the planar locomotion, the velocity ${}^k\boldsymbol{u}_i(t)$ at the kth point on the ith cell in the laboratory frame can be represented by

$${}^k\boldsymbol{u}_i(t) = {}^k\boldsymbol{v}_i(t) + {}^k\boldsymbol{\mathsf{B}}_i(t)\,\mathcal{U}(t), \tag{4.2}$$

where

$$\mathcal{U} = \begin{bmatrix} U_x \\ U_y \\ \varOmega_1 \\ \varOmega_2 \\ F^{\mathrm{a}}_{21x} \\ F^{\mathrm{a}}_{21y} \end{bmatrix}, \qquad {}^k\boldsymbol{\mathsf{B}}_i = \begin{cases} \begin{bmatrix} 1 & 0 & -{}^kr'_{1y} & 0 & 0 & 0 \\ 0 & 1 & {}^kr'_{1x} & 0 & 0 & 0 \\ 0 & 0 & 0 & 0 & 0 & 0 \end{bmatrix}, & i=1, \\ \begin{bmatrix} 1 & 0 & 0 & -{}^kr'_{2y} & 0 & 0 \\ 0 & 1 & 0 & {}^kr'_{2x} & 0 & 0 \\ 0 & 0 & 0 & 0 & 0 & 0 \end{bmatrix}, & i=2. \end{cases} \tag{4.3}$$

Here, the subscripts x and y in the variables represent their components along the x- and y-axes, respectively. The angular speeds $\varOmega_1$ and $\varOmega_2$ are defined such that $\boldsymbol{\varOmega}_1 = \varOmega_1\boldsymbol{e}_3$ and $\boldsymbol{\varOmega}_2 = \varOmega_2\boldsymbol{e}_3$, where $\boldsymbol{e}_3 = \boldsymbol{e}_1 \times \boldsymbol{e}_2$.

The microscale geometry and swimming speed of spermatozoa render them low-Reynolds-number swimmers. They are generally deemed neutrally buoyant, as their swimming speed dominates their sedimentation speed (Gong *et al.* 2020). Consequently, the swimming paired sperm cells are force-free and torque-free (Lauga & Powers 2009). The ith cell in a sperm pair satisfies

$$\int_s \boldsymbol{f}_i(s,t)\,\mathrm{d}s + \boldsymbol{F}^{\mathrm{a}}_{ij}(t) = \boldsymbol{0}, \qquad \int_s \boldsymbol{r}_i(s,t) \times \boldsymbol{f}_i(s,t)\,\mathrm{d}s + \boldsymbol{T}^{\mathrm{a}}_{ij}(t) = \boldsymbol{0}, \tag{4.4}$$

where $\boldsymbol{f}_i(s,t)$ is the hydrodynamic force at point $\boldsymbol{r}_i(s,t)$, as illustrated in figure 1. The adhesive torque on the ith head about the origin of the laboratory frame is $\boldsymbol{T}^{\mathrm{a}}_{ij} = \boldsymbol{r}_{\mathrm{p}} \times \boldsymbol{F}^{\mathrm{a}}_{ij}$. The total torque balances about any point.

The loss modulus of the fluid in our experiments dominates the storage modulus (Morcillo i Soler *et al.* 2022; Zhang *et al.* 2023). Consequently, we can neglect the elasticity of the fluid and calculate the hydrodynamic force $\boldsymbol{f}_i(s,t)$ using Stokes equations. To incorporate the wall effect due to the top and bottom slides of the chamber, we introduce two walls in our models, which are at $z = 0\ \mu\mathrm{m}$ and $z = 20\ \mu\mathrm{m}$, respectively, parallel with the x–y plane. According to previous studies, most spermatozoa are within 0.2 times their body length from the bottom surface (Winet *et al.* 1984; Elgeti *et al.* 2011). We therefore assume that the sperm cells are in the middle between the walls in our models. In the experiments, the sperm heads are physically attached. In the models, they need to be prevented from concurrently occupying the same space. Therefore, a pair of sperm cells is positioned on two parallel two-dimensional planes, with minimum distance $0.25\ \mu\mathrm{m}$ between their heads. Given that the height of the head is $0.4\ \mu\mathrm{m}$, the two swimming planes are set at $z = 9.675\ \mu\mathrm{m}$ and $z = 10.325\ \mu\mathrm{m}$, respectively. This arrangement ensures that the two cells remain in close proximity without overlapping in space.

To determine the hydrodynamic force $\boldsymbol{f}_i$ on the ith cell, we use the regularised Stokeslets method, which is an effective approximation of the low-Reynolds-number flow.

We discretise the ith cell into n_i points, and the walls into n_{w} points, as detailed in Appendix A. Thus a total of $n = n_1 + n_2 + n_{\mathrm{w}}$ points are included in our models. The relationship between the force $\boldsymbol{f}_i$ and the velocity $\boldsymbol{u}_i$ can be expressed in a vector form

$$\left[\boldsymbol{u}_1^{\mathrm{T}} \quad \boldsymbol{u}_2^{\mathrm{T}} \quad \boldsymbol{u}_w^{\mathrm{T}}\right]^{\mathrm{T}} = -\boldsymbol{A}\left[\boldsymbol{f}_1^{\mathrm{T}} \quad \boldsymbol{f}_2^{\mathrm{T}} \quad \boldsymbol{f}_{\mathrm{w}}^{\mathrm{T}}\right]^{\mathrm{T}}, \tag{4.5}$$

where $\boldsymbol{f}_{\mathrm{w}}$ is the hydrodynamic force on the stationary wall surfaces, and $\boldsymbol{A}$ is a $3n \times 3n$ matrix (Appendix B). The velocity of the n_{w} points on the wall surfaces $\boldsymbol{u}_{\mathrm{w}}$ can be specified by a $3n_{\mathrm{w}} \times 1$ zero matrix, $\boldsymbol{u}_{\mathrm{w}} = \boldsymbol{0}_{3n_{\mathrm{w}}\times 1}$. Combining (4.2)–(4.5), we derive a linear system to describe the dynamics of paired sperm cells,

$$\begin{bmatrix} \boldsymbol{v} \\ 0 \\ 0 \\ 0 \\ 0 \\ 0 \\ 0 \end{bmatrix} = -\begin{bmatrix} \boldsymbol{A} & \boldsymbol{B} \\ \boldsymbol{C} & \boldsymbol{D} \\ \boldsymbol{E} & \boldsymbol{F} \\ \boldsymbol{G} & \boldsymbol{H} \\ \boldsymbol{I} & \boldsymbol{J} \\ \boldsymbol{K} & \boldsymbol{L} \\ \boldsymbol{M} & \boldsymbol{N} \end{bmatrix} \begin{bmatrix} \boldsymbol{f} \\ \mathcal{U} \end{bmatrix}, \tag{4.6}$$

where $\boldsymbol{B} = [{}^1\boldsymbol{B}_1^{\mathrm{T}} \quad {}^2\boldsymbol{B}_1^{\mathrm{T}} \quad \cdots \quad {}^{n_1}\boldsymbol{B}_1^{\mathrm{T}} \quad {}^1\boldsymbol{B}_2^{\mathrm{T}} \quad {}^2\boldsymbol{B}_2^{\mathrm{T}} \cdots \quad {}^{n_2}\boldsymbol{B}_2^{\mathrm{T}} \quad \boldsymbol{0}_{6\times 3n_{\mathrm{w}}}]^{\mathrm{T}}$, the velocity is $\boldsymbol{v} = [\boldsymbol{v}_1^{\mathrm{T}} \quad \boldsymbol{v}_2^{\mathrm{T}} \quad \boldsymbol{0}_{1\times 3n_{\mathrm{w}}}]^{\mathrm{T}}$, and the force is $\boldsymbol{f} = [\boldsymbol{f}_1^{\mathrm{T}} \quad \boldsymbol{f}_2^{\mathrm{T}} \quad \boldsymbol{f}_{\mathrm{w}}^{\mathrm{T}}]^{\mathrm{T}}$. The last six equations in (4.6) represent the force balance along the x- and y-axes, and the torque balance along the z-axis, respectively, for each pair of sperm cells. According to the force-balance and torque-balance conditions, the blocks $\boldsymbol{C}$, $\boldsymbol{D}$, …, $\boldsymbol{N}$ of this linear system can be derived (Appendix C). In (4.6), velocity $\boldsymbol{v}$ at any time is known, which is provided from experimental observations, but $\boldsymbol{f}$ and all the variables in $\mathcal{U}$ are unknown and need to be determined from (4.6). The velocity $\boldsymbol{u}_i$ at any point on the ith sperm pair with respect to the laboratory frame can be further calculated from (4.2) after $\mathcal{U}$ is determined.

4.2. *Model of paired spermatozoa with adhesive and steric forces between their heads*

To prevent sperm cells from unrealistically passing through each other, a steric force has been introduced and modelled as an elastic spring with a specific form (Cripe *et al.* 2016; Simons & Rosenberger 2021). The steric force in their model acts only over a very short range to avoid significantly influencing sperm swimming. Likewise, instead of focusing on the specific value of steric force, we expect that the steric force in our model 2 can effectively repel the heads when they approach a total overlap, while having a minimum influence on their relative oscillation when their orientation difference is $\Delta\alpha > 0$. To this end, we develop model 2 based on model 1. We first consider a scenario in which both heads have the same angular velocity, i.e. $\boldsymbol{\Omega}_1 = \boldsymbol{\Omega}_2 = \boldsymbol{\Omega}$. The velocity ${}^k\boldsymbol{u}_i(t)$ at the kth point on the ith cell in the laboratory frame can continue to be represented by (4.2), but the matrices $\mathcal{U}$ and ${}^k\boldsymbol{B}_i$ need to be modified to

$$\mathcal{U}' = \begin{bmatrix} U_x \\ U_y \\ \Omega \end{bmatrix}, \quad {}^k\boldsymbol{B}_i' = \begin{bmatrix} 1 & 0 & -{}^k r_{iy}' \\ 0 & 1 & {}^k r_{ix}' \\ 0 & 0 & 0 \end{bmatrix}, \quad i = 1, 2, \tag{4.7}$$

respectively. As $\boldsymbol{F}_{12}^{\mathrm{a}} = -\boldsymbol{F}_{21}^{\mathrm{a}}$ and $\boldsymbol{F}_{12}^{\mathrm{s}} = -\boldsymbol{F}_{21}^{\mathrm{s}}$, the force-balance and torque-balance conditions on the whole sperm pair are

$$\sum_{i=1}^{2} \int_s \boldsymbol{f}_i(s, t)\, \mathrm{d}s = \boldsymbol{0}, \quad \sum_{i=1}^{2} \int_s \boldsymbol{r}_i(s, t) \times \boldsymbol{f}_i(s, t)\, \mathrm{d}s = \boldsymbol{0}. \tag{4.8}$$

Algorithm 1. Model 2.

```
Input: $\boldsymbol{v}$, $\boldsymbol{r}(t_1)$, $\Delta\alpha(t_1)$
Output: $\boldsymbol{r}(t_j)$, $\Delta\alpha(t_j)$, $\boldsymbol{f}(t_j)$, $\boldsymbol{U}(t_j)$, $\boldsymbol{\Omega}_1(t_j)$, $\boldsymbol{\Omega}_2(t_j)$

$j \leftarrow 1$;
while $j \leqslant n_t$ do
    $j \leftarrow j + 1$;
    Get $\boldsymbol{r}(t_j)$, $\Delta\alpha(t_j)$, $\boldsymbol{f}(t_j)$, $\boldsymbol{U}(t_j)$, $\boldsymbol{\Omega}_1(t_j)$, $\boldsymbol{\Omega}_2(t_j)$ from equation (4.6);
    if $\Delta\alpha(t_j) \leqslant 0$ then
        Get $\boldsymbol{r}(t_j)$, $\Delta\alpha(t_j)$, $\boldsymbol{f}(t_j)$, $\boldsymbol{U}(t_j)$, $\boldsymbol{\Omega}_1(t_j)$, $\boldsymbol{\Omega}_2(t_j)$ from equation (4.9);
    end
end
```

Combining (4.2), (4.5), (4.7) and (4.8), we derive a linear system to describe the dynamics of paired sperm cells with the same head angular velocity $\boldsymbol{\Omega}$,

$$\begin{bmatrix} \boldsymbol{v} \\ 0 \\ 0 \\ 0 \end{bmatrix} = - \begin{bmatrix} \boldsymbol{A} & \boldsymbol{B}' \\ \boldsymbol{C}' & \boldsymbol{D}' \\ \boldsymbol{E}' & \boldsymbol{F}' \\ \boldsymbol{G}' & \boldsymbol{H}' \end{bmatrix} \begin{bmatrix} \boldsymbol{f} \\ \mathcal{U}' \end{bmatrix}, \tag{4.9}$$

where $\boldsymbol{B}' = [{}^1\boldsymbol{B}_1'^{\mathrm{T}}\ {}^2\boldsymbol{B}_1'^{\mathrm{T}} \ldots {}^{n_1}\boldsymbol{B}_1'^{\mathrm{T}}\ {}^1\boldsymbol{B}_2'^{\mathrm{T}}\ {}^2\boldsymbol{B}_2'^{\mathrm{T}} \ldots {}^{n_2}\boldsymbol{B}_2'^{\mathrm{T}}\ \boldsymbol{0}_{3\times 3n_{\mathrm{w}}}]^{\mathrm{T}}$, the velocity is $\boldsymbol{v} = [\boldsymbol{v}_1^{\mathrm{T}}\ \boldsymbol{v}_2^{\mathrm{T}}\ \boldsymbol{0}_{1\times 3n_{\mathrm{w}}}]^{\mathrm{T}}$, and the force is $\boldsymbol{f} = [\boldsymbol{f}_1^{\mathrm{T}}\ \boldsymbol{f}_2^{\mathrm{T}}\ \boldsymbol{f}_{\mathrm{w}}^{\mathrm{T}}]^{\mathrm{T}}$. The last three equations in (4.9) represent the force balance along the x- and y-axes, and the torque balance along the z-axis, for the sperm pair, respectively. According to the force-balance and torque-balance conditions, the blocks $\boldsymbol{C}'$, $\boldsymbol{D}'$, ..., $\boldsymbol{H}'$ of this linear system can be derived (Appendix D). In (4.9), velocity $\boldsymbol{v}$ at any time is known, which is provided from experimental observations, but $\boldsymbol{f}$ and all the variables in $\mathcal{U}'$ are unknown and need to be determined from (4.9). The velocity $\boldsymbol{u}_i$ at any point on the ith sperm pair with respect to the laboratory frame can be further calculated from (4.2) after $\mathcal{U}'$ is determined.

Our simulation consists of n_t discrete time steps. If at the beginning of the jth time step, the position $\boldsymbol{r}(t_j)$ of any point on the surface of the sperm cells and the velocity $\boldsymbol{v}(t_j)$ are known, then $\boldsymbol{r}(t_{j+1})$, $\Delta\alpha(t_{j+1})$, $\boldsymbol{f}(t_{j+1})$, $\boldsymbol{U}(t_{j+1})$, $\boldsymbol{\Omega}_1(t_{j+1})$ and $\boldsymbol{\Omega}_2(t_{j+1})$ at the beginning of the $(j+1)$th time step can be determined by solving (4.6) or (4.9). In our simulations, the initial position $\boldsymbol{r}(t_1)$ is given, and the velocity $\boldsymbol{v}$ at any time step is provided from experimental observations. Assuming that the initial orientation difference between the heads is $\Delta\alpha(t_1) \geq 0$, now we can formulate model 2 by combining (4.6) and (4.9) following the method described in Algorithm 1.

In model 2 (i.e. Algorithm 1), sperm heads are fused with zero relative angular velocity, $\Delta\boldsymbol{\Omega} = \boldsymbol{\Omega}_2 - \boldsymbol{\Omega}_1 = \boldsymbol{0}$, when $\Delta\alpha$ is within a very small range close to zero. This range depends on the variation of $\Delta\alpha$ over one discrete time step. Note that both adhesive and steric forces between the heads are intrinsically included in model 2, constraining the relative oscillation of the heads such that $\Delta\boldsymbol{\Omega} = \boldsymbol{0}$ when $\Delta\alpha$ is within the range, despite the specific values of the forces and where they are applied being unknown. Only an adhesive force between the heads is included in model 2 when $\Delta\alpha$ is out of the range. Thereby, we finish developing model 2, in which sperm heads are effectively prevented from totally overlapping, while having a minimum influence on their relative oscillation when $\Delta\alpha > 0$.

4.3. *Validation of the models*

Model 3 can be developed based on model 1 (i.e. (4.6)) by reducing the vector $\mathcal{U}$ in model 1 to $\mathcal{U} = [U_x\ U_y\ F^{\mathrm{a}}_{21x}\ F^{\mathrm{a}}_{21y}]^{\mathrm{T}}$ and removing the two equations associated with the torque-balance condition from (4.6). Our models build on regularised Stokeslets method, involving a choice of regularised parameter ϵ and spatial discretisation of the sperm cells and walls. To validate our discretisation of the head and flagellum, following the approach of Cortez *et al.* (2005) and Gillies *et al.* (2009), we compare our predicted resistive force on an isolated head and an isolated flagellum translating in an unbounded fluid with their exact solution. The non-dimensional force error is $e_{\mathrm{f}} < 2.4 \times 10^{-4}$ (Appendix E). In addition, we compute the cumulative distribution of velocity error for a sphere translating in an unbounded fluid with velocity $U_z = 1\ \mathrm{m\,s^{-1}}$. All the points on the surface of the sphere have a velocity error $e_{\mathrm{v}} = |U_z - 1| < 0.018\ \mathrm{m\,s^{-1}}$ (Appendix E). To regularise the walls in our models, the regularised parameter ϵ is chosen in the form $\epsilon = \xi \rho^m$ (Ainley *et al.* 2008; Gillies *et al.* 2009). In our test cases, $\xi = 0.5$ and $m = 0.9$ are chosen, which yields predictions that closely match the published results (Appendix F). Therefore, these values of ξ and m are used in our models for all subsequent simulations. The walls in our models are square. The simulations in the test cases are insensitive to the wall size when the side length of the walls ranges from 60 to 160 µm, as shown in Appendix F. Therefore, the side length of each wall is set to 80 µm in our models, which is fixed in all our subsequent simulations.

4.3.1. *Force and torque errors*

We use our models to simulate the locomotion of a sperm pair. In the simulations, the viscosity is chosen as $\mu = 1$ Pa s, and the flagellar beat patterns are prescribed based on the experimental measurements. For model 3, prescribed head angular velocities $\boldsymbol{\varOmega}_i(t)$, $i = 1, 2$, are further required.

Regarding models 1 and 2, force-balance conditions along the x- and y-axes and torque-balance conditions along the z-axis are applied. As the mechanical coupling between the heads is a pair of internal forces, the total hydrodynamic force on the whole sperm pair along the x- and y-axes should satisfy $F_x = \sum_{i=1}^{2} F_{ix} = 0$ and $F_y = \sum_{i=1}^{2} F_{iy} = 0$, where F_{ix} and F_{iy} are the x- and y-components of the total hydrodynamic force on the ith cell, respectively. Likewise, the total hydrodynamic torque on the whole sperm pair along the z-axis should satisfy $T_z = \sum_{i=1}^{2} T_{iz} = 0$, where T_{iz} is the z-component of the total hydrodynamic torque on the ith cell. As shown in figure 2, the absolute values $|F_x|$, $|F_y|$ and $|T_z|$ are minimal. The minimal values result from the numerical error. The absolute value of the total hydrodynamic force on the sperm pair along the z-axis, $|F_z|$, is also very small. We take the total hydrodynamic force on cell 1, $|F_1|$, as the benchmark, and $|F_z|$ is three orders of magnitude lower than $|F_1|$, despite no force-balance condition along the z-axis applied to the sperm cells. Likewise, taking $|T_1|$ as the benchmark, the absolute values of the total hydrodynamic torque on the sperm pair along the x- and y-axes, $|T_x|$ and $|T_y|$, are three orders of magnitude lower than $|T_1|$, despite no torque-balance conditions along the x- and y-axes applied to the sperm cells.

Regarding model 3, force-balance conditions along the x- and y-axes are applied to the sperm cells. The absolute values $|F_x|$ and $|F_y|$ are minimal due to the numerical error, as shown in figure 2(*a*,*iii*). In addition, $|F_z|$ is three orders of magnitude lower than $|F_1|$, and $|T_x|$, $|T_y|$ and $|T_z|$ are three orders of magnitude lower than $|T_1|$, despite no force-balance condition along the z-axis and no torque-balance conditions along the x-, y- and z-axes applied to the sperm pair.

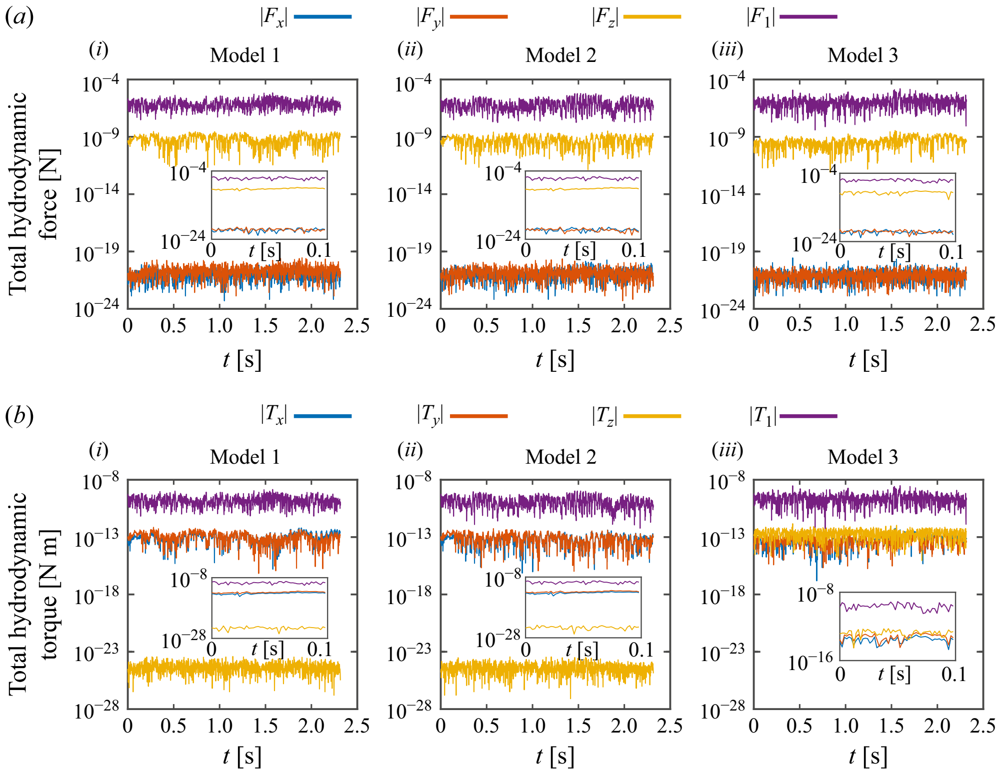

Figure 2. (*a*) The absolute values of the *x*-, *y*- and *z*-components of the total hydrodynamic force on a sperm pair in models 1 (*i*), 2 (*ii*), and 3 (*iii*) are minimal compared to the absolute value of the total hydrodynamic force on cell 1 of this sperm pair, $|F_1|$. (*b*) The absolute values of the *x*-, *y*- and *z*-components of the total hydrodynamic torque on the sperm pair in models 1 (*i*), 2 (*ii*), and 3 (*iii*) are minimal compared to the absolute value of the total hydrodynamic torque on cell 1 of this sperm pair, $|T_1|$. The force and torque components during a shorter time range, 0–0.1 s, are shown in the insets.

4.3.2. *Comparison of the predicted and experimentally observed trajectories of sperm pairs*

Following previous studies (Yundt *et al.* 1975; Gillies *et al.* 2009), we assess our models by comparing the predicted and experimentally observed swimming trajectories. Three sperm pairs are simulated using our models. The trajectory of each sperm pair is the time-varying position of their pivot point, as shown in figure 3. We calculate the displacement d and travelling distance S of the pivot point during one flagellar beat cycle T. The displacement during the jth flagellar beat cycle d is defined as

$$d = \frac{1}{n_t} \sum_{i=1}^{n_t} \left| \boldsymbol{r}_p(t_i + T) - \boldsymbol{r}_p(t_i) \right| , \tag{4.10}$$

where n_t is the number of the time steps during one flagellar beat cycle T. The displacement $|\boldsymbol{r}_p(t_i + T) - \boldsymbol{r}_p(t_i)|$ depends on the initial time t_i during one beat cycle. We thus define d by averaging $|\boldsymbol{r}_p(t_i + T) - \boldsymbol{r}_p(t_i)|$ over one beat cycle using (4.10). The travelling distance of the pivot point during the jth flagellar beat cycle S is defined as $S = \sum_{i=1}^{n_t} \left| \boldsymbol{r}_p(t_i) - \boldsymbol{r}_p(t_{i-1}) \right|$. Taking sperm pair 3, for example (figure 3*e*), there are 40 flagellar beat cycles. Compared with the experimentally observed displacement averaged over 40 flagellar beat cycles $\langle d_{obse} \rangle$, the predicted one, $\langle d_{theo} \rangle$, in models 1, 2 and

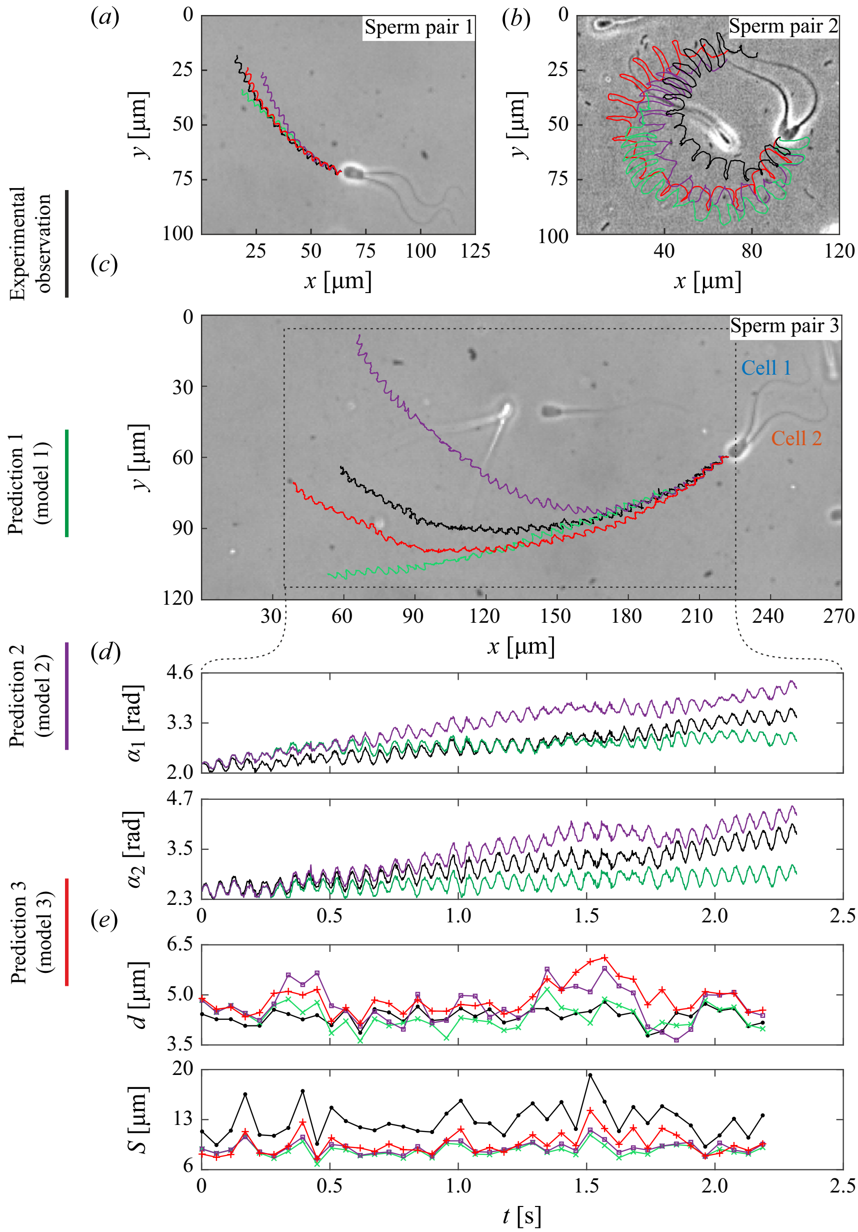

Figure 3. Three sperm pairs, referred to as (*a*) sperm pair 1, (*b*) sperm pair 2, and (*c*) sperm pair 3, were tracked using high-speed videomicroscopy. In each sperm pair, the trajectory of the pivot point is predicted using models 1, 2 and 3, respectively. (*d*) The head orientations of cell 1 (α_1) and cell 2 (α_2) in sperm pair 3 are time-varying. Orientations in model 3 overlap with the experimentally measured ones. (*e*) Regarding the pivot point in sperm pair 3, the predictions and experimental observation have similar tendencies in the displacement d. The predictions and experimental observation have similar tendencies in the travelling distance S.

3, is 0.2 % shorter, 7.8 % longer, and 11.7 % longer, respectively. The predicted travelling distances of the pivot point averaged over the 40 beat cycles, $\langle S_{theo} \rangle$, in models 1, 2 and 3 are 32.1 %, 29.4 % and 25.1 %, respectively, shorter than the experimentally observed one $\langle S_{obse} \rangle$.

In our experiments, the trajectory of the pivot point wiggles around its average path, resulting in the time-varying longitudinal and lateral displacement within one flagellar beat cycle. Our models predict the fine structure of the locomotion of the sperm pairs such as the wiggling. However, the agreement between the predicted and experimentally observed swimming trajectories varies significantly between the models. We quantify the agreement between the predicted and experimentally observed trajectories using Fréchet distance d_{Fr}, a lower value of which indicates a higher similarity (Eiter & Mannila 1994). Taking sperm pair 3, for example, compared with the experimentally observed swimming trajectory, d_{Fr} is 45.6, 56.6 and 21.1 μm for the predicted trajectory in models 1, 2 and 3, respectively. As shown in figure 3*c*, compared with models 1 and 2, model 3 predicts a trajectory with higher similarity to the experimentally observed one, revealing the significant role of head oscillation in the swimming trajectory of sperm pairs. The improved prediction accuracy results from the available correct information, i.e. the head angular velocities.

5. Swimming performances of paired spermatozoa

In our experiments, paired sperm cells beat their two flagella with the same period, exhibiting different modes of flagellar synchronisation, as shown in figure 4(*a*). To formalise the locomotion of the paired spermatozoa, the high-dimensional description of flagellar beating by (3.1) can be further mapped to a low-dimensional space spanned by the first two shape scores β_1 and β_2 using principal component analysis (Geyer *et al.* 2013; Werner *et al.* 2014). The points in the (β_1, β_2) space represent a series of flagellar shapes and form a closed loop (figure 4*b*). We define a limit cycle of the beating of the *i*th flagellum by fitting the closed loop parametrised by a phase ϕ_i (Appendix G). The flagellar phase ϕ_i is defined according to flagellar shape similarity such that it is independent of its time derivative, whereby a unique phase is assigned for each tracked flagellar shape (Geyer *et al.* 2013). Accordingly, a swimming sperm pair can be completely characterised with the position of the pivot point $\boldsymbol{r}_{\mathrm{p}}$, the orientation of the heads α_i, and the phase of flagellar beating ϕ_i. The flagellar synchronisation of paired cells is achieved when the phase lag between their flagellar beating $\Delta\phi = \phi_2 - \phi_1$ remains unchanged over one beat cycle. The sperm pairs were observed experimentally to maintain a constant flagellar phase lag $\Delta\phi$ for several beat cycles, followed by phase slips, and then establish another constant flagellar phase lag, as shown in figure 4(*c*). This repeated process allowed the flagellar synchronisation to transition between in-phase, anti-phase and lagged synchronisation.

Inspired by the experimental observations, we further investigate numerically the influence of the flagellar phase lag $\Delta\phi$ on the swimming of paired cells. Both models 1 and 2 are used in our simulations. In our simulations, the flagellar beat patterns are reconstructed from their limit cycles (Appendix G). The phase-lag dependence of flagellar waveforms is neglected. We assess the swimming performances of sperm pairs regarding three parameters: average swimming speed $\langle U \rangle$, average power consumption $\langle P \rangle$, and swimming efficiency η. In our simulations, the three parameters are determined after the sperm pair has established regular beating, when its displacement during one flagellar beat cycle, d, stops varying between beat cycles. The average swimming speed over one beat cycle is determined by $\langle U \rangle = d/T$, representing the swimming speed along the average path. Here, d is calculated using (4.10). The average power consumption per cell $\langle P \rangle$ for a sperm pair is determined by averaging the instantaneous power of cells 1 and 2 over one beat cycle (Appendix H). Compared to speed, swimming efficiency η may be more critical for spermatozoa due to their limited energy reserves. We define $\eta = \langle U \rangle^2 / \langle P \rangle$. This means that a longer swimming displacement per unit of energy consumption leads to higher efficiency. Given other conditions (e.g. the flagellar waveform due to the viscosity)

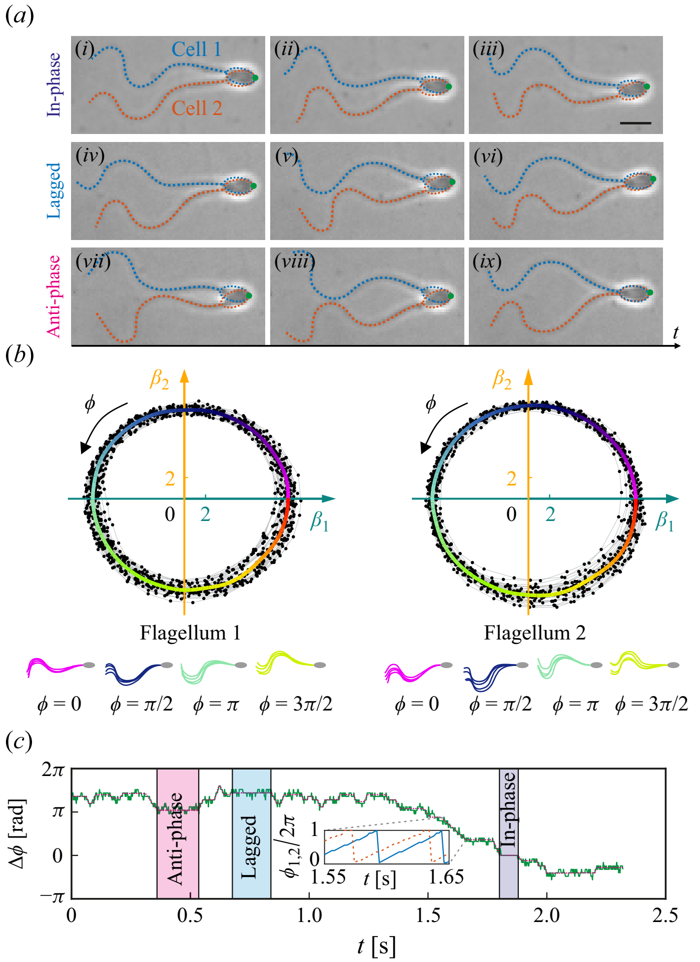

Figure 4. A swimming sperm pair was observed experimentally to exhibit three different modes of flagellar synchronisation: in-phase, anti-phase and lagged synchronisation. (*a*) Interrupted by phase slips, the sperm pair transitioned between the modes of flagellar synchronisation. Scale bar: 10 µm. (*b*) To characterise the flagellar beating, their shapes are mapped into a two-dimensional space spanned by the first two shape scores β_1 and β_2. The phase of the flagellar beating is obtained through binning tracked flagellar shapes according to shape similarity. (*c*) The phase lag between the flagella of the sperm pair $\Delta\phi$ is unwrapped and clearly shows the phase lags, slips and synchronisation. Inset: the flagellar phases ϕ_1 and ϕ_2 during a time interval when phase slips occur.

unchanged, $\langle U \rangle$ is independent of fluid viscosity μ, whereas the average power $\langle P \rangle$ depends linearly on it, and η has an inverse dependence on it. To compare $\langle P \rangle$ and η at different fluid viscosities and various flagellar phase lags, we use $\mu = 1$ Pa s in all our simulations for swimming performances, and normalise η with its value at $\Delta\phi = 0$, denoted by η_0.

In all our simulations for swimming performances, the period of flagellar beating is the same for the cells within a sperm pair, but distinct among the pairs. The flagellar waveform varies between the pairs. Therefore, sperm pairs with the same flagellar phase lag exhibit distinct swimming performances, as shown in figure 5. In addition, a small variation in $\Delta\phi$ may lead the swimming performances to change significantly, especially for η/η_0 when the value of $\langle P \rangle$ is small. For instance, the value of η/η_0 for sperm pair 2 in

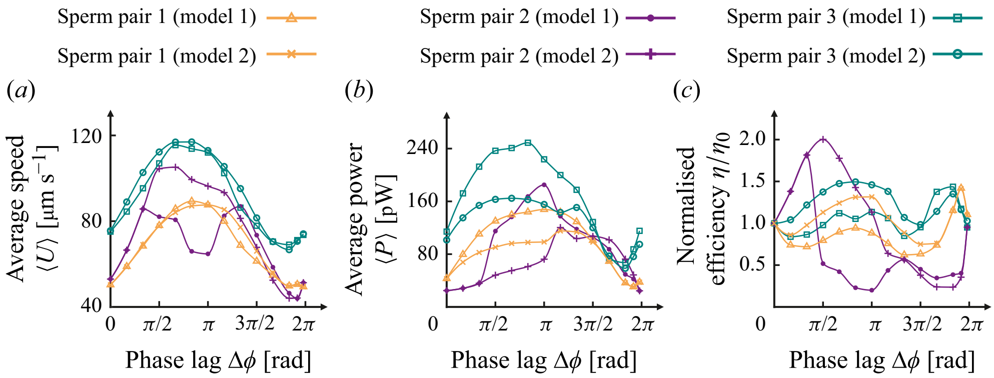

Figure 5. Three distinct sperm pairs respond differently to the flagellar phase lag $\Delta\phi$ in (*a*) average swimming speed $\langle U \rangle$, (*b*) swimming power $\langle P \rangle$, and (*c*) normalised swimming efficiency η/η_0. Here, η_0 is the efficiency when $\Delta\phi = 0$. Models 1 and 2 are used to calculate $\langle U \rangle$, $\langle P \rangle$ and η/η_0 for each sperm pair. Each simulation includes 14 different values of flagellar phase lag $\Delta\phi$: 0, $\pi/6$, $\pi/3$, $\pi/2$, $2\pi/3$, $5\pi/6$, π, $7\pi/6$, $4\pi/3$, $3\pi/2$, $5\pi/3$, $11\pi/6$, $23\pi/12$ and $95\pi/48$.

model 1 significantly increases from 0.40 to 0.95 as $\Delta\phi$ increases from $23\pi/12$ to $95\pi/48$ (figure 5*c*). In all our simulations for swimming performances, compared with the small flagellar phase lags (approximately 0 radians), large flagellar phase lags (approximately π radians) lead to a higher $\langle P \rangle$, which aligns with previous studies (Elfring & Lauga 2011*a*; Cripe *et al.* 2016). However, a high swimming speed or efficiency does not necessarily result from flagellar phase lags close to π radians. For instance, in model 2, sperm pair 2 achieves its highest $\langle U \rangle$ and η/η_0 when its flagellar phase lag $\Delta\phi$ is close to $\pi/2$ radians. In addition, the swimming performances are influenced significantly by the mechanical head–head coupling. For the same sperm pair with the same $\Delta\phi$ but different head–head coupling, it may have a large difference in $\langle U \rangle$, $\langle P \rangle$ or η/η_0, as shown in figure 5. Taking sperm pair 2, for example, when $\Delta\phi = \pi/3$, the value of $\langle U \rangle$ in model 1 is equal to that in model 2. But when $\Delta\phi = \pi/2$, the value of $\langle U \rangle$ for sperm pair 2 in model 1 diverges significantly from that in model 2. One reason is that the orientation difference between the heads $\Delta\alpha(t)$ is constrained in model 2 such that $\Delta\alpha(t) \geq 0$ for the whole course of swimming, whereas no such constraint exists in model 1, as shown in figure 6(*a*). This constraint in the relative head oscillation leads to different swimming trajectories, as shown in figure 6(*b*). However, in our experiments, we did not observe the sperm pairs with their head orientation difference at $\Delta\alpha(t) < 0$ during swimming. Therefore, steric force probably exists between the heads of the sperm pairs in the experiments, repelling each other.

Furthermore, the flagellar waveform also varies between the cells in the same sperm pair, resulting in a difference in the power $\langle P_1 \rangle$ and $\langle P_2 \rangle$, as shown in figure 7. In our simulations, $\langle P \rangle$ for each sperm pair is always a positive value. But for sperm pair 2 in model 1, the average power for cell 1 is $\langle P_1 \rangle = -5.5$ pW when $\Delta\phi = 23\pi/12$, as shown in figure 7(*b*).

6. Discussion

The collective behaviours of mechanically and hydrodynamically coupled flagellated cells are complex and not fully understood. Here, using paired bovine spermatozoa as an example, we develop hydrodynamic models to unveil more nuanced aspects of their locomotion. Compared to current theoretical models, our models offer some advantages

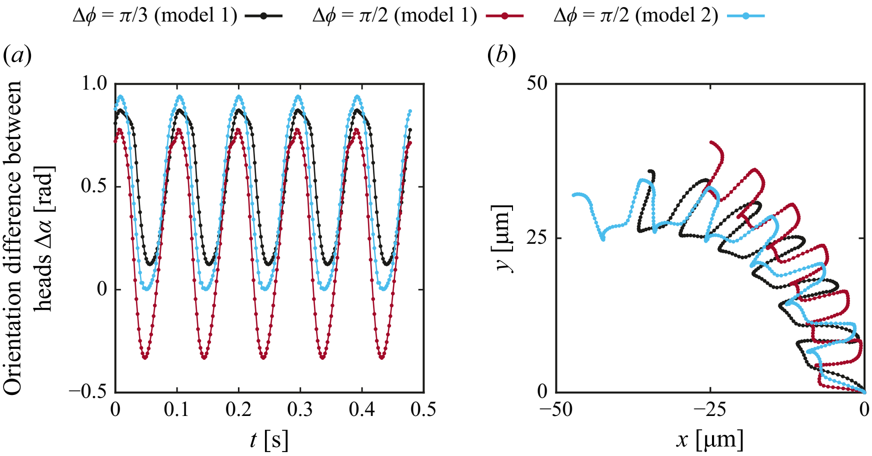

Figure 6. For sperm pair 2, (*a*) its head orientation difference $\Delta\alpha(t)$ and (*b*) its swimming trajectories during five flagellar beat cycles are shown. When $\Delta\phi = \pi/3$, sperm pair 2 in models 1 and 2 has the same time-varying $\Delta\alpha(t)$. When $\Delta\phi = \pi/2$, the head orientation difference $\Delta\alpha(t)$ for sperm pair 2 in model 1 can be a negative value within a time interval, during which the relative oscillation of the heads of sperm pair 2 in model 2 are fused such that their relative angular speed is $\Delta\Omega = 0$.

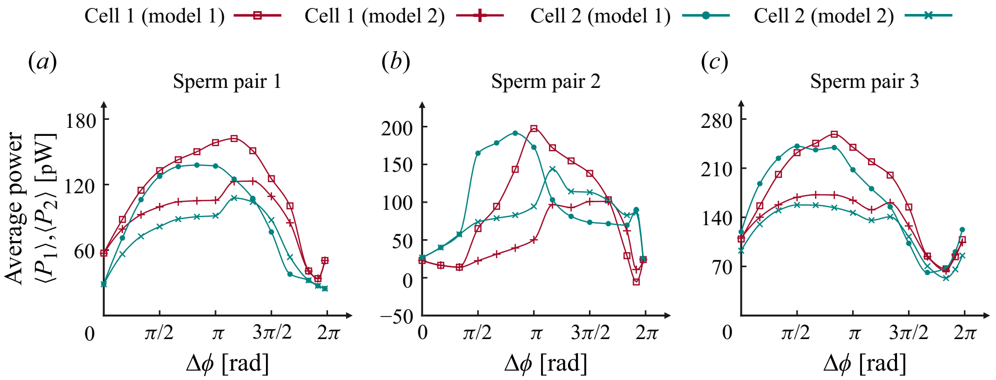

Figure 7. Sperm pairs (*a*) 1, (*b*) 2 and (*c*) 3 are shown. Models 1 and 2 are used to calculate the average power consumption for cell 1 ($\langle P_1\rangle$) and cell 2 ($\langle P_2\rangle$) in each sperm pair. Each simulation includes 14 different values of flagellar phase lag $\Delta\phi$: 0, $\pi/6$, $\pi/3$, $\pi/2$, $2\pi/3$, $5\pi/6$, π, $7\pi/6$, $4\pi/3$, $3\pi/2$, $5\pi/3$, $11\pi/6$, $23\pi/12$ and $95\pi/48$.

for accurate predictions. First, our models include sperm heads, which are often missing in current models for attached or detached sperm cells (Cripe *et al.* 2016; Simons & Rosenberger 2021; Carichino *et al.* 2021). In addition, we consider both the mechanical and hydrodynamic cell–cell interactions, whereas only one type of interaction has typically been incorporated in current theoretical models (Pearce *et al.* 2018; Carichino *et al.* 2021).

Our simulations show that the mechanical head–head coupling significantly affects the swimming trajectory of sperm pairs (figures 3 and 6). The head orientations α_1 and α_2 are history-dependent, while the displacement d and travelling distance S are not. The time-dependent trajectory of paired spermatozoa is sensitive to the initial values of their head orientation, angular velocity and translational velocity. A small variation in the initial values would lead to a significant cumulative error in the predicted trajectory. Comparing the predictions in the displacement during one beat cycle d with the experimentally observed ones, we find that both underpredictions and overpredictions appear in our simulations, depending on models and sperm pairs (figure 3). In a previous computational study for single sperm cells, only underpredictions in d were found (Gillies *et al.* 2009). In our simulations, the discrepancy in the displacement d between the predictions and experimental observations likely results from the missing information in the environment and flagella. For instance, we postulate that the sperm pairs swim in the middle plane between the walls, which may not align with reality. Closer proximity of sperm cells to the wall surface results in higher swimming speed (Smith *et al.* 2009). Additionally, although our mathematical models treat flagellar beating as planar, it is not strictly planar in reality, particularly at the distal end of the flagellum. A slight tilt of the planar motion out of the swimming plane may contribute to the discrepancy. Another potential contributor is the missing information on whether sperm pairs come into contact with the chamber walls transiently.

Correct information, e.g. the time-varying angular velocities of heads, improves the accuracy in predicting the trajectory of sperm pairs. However, the underlying mechanism of the mechanical head–head coupling is not fully understood, limiting our prediction accuracy. The trajectory of each sperm pair during one beat cycle differs from that during another beat cycle. Such seemingly stochastic swimming has also been observed experimentally in individual sperm cells and is attributed to the active phase and amplitude fluctuations of flagellar beating (Ma *et al.* 2014). In the case of paired spermatozoa, cell–cell interactions are another contributor. The combined effects of flagellar fluctuations and cell–cell interactions are also reflected in the radial distribution of the points around the closed loop (figure 4*b*).

Three different modes of flagellar synchronisation were observed in our experiments, reminiscent of the similar flagellar beat patterns found in *Chlamydomonas* (Leptos *et al.* 2013; Wan *et al.* 2014; Quaranta *et al.* 2015; Wan & Goldstein 2016) and model microfilaments (Guo *et al.* 2018,2021). Current models focus primarily on flagellar synchronisation at a rigid/elastic base, using either low-order representations of flagella as oscillators (Uchida & Golestanian 2011; Golestanian *et al.* 2011; Klindt *et al.* 2017; Hickey *et al.* 2023) or more realistic representations as elastic beams (Riedel-Kruse *et al.* 2007; Osterman & Vilfan 2011; Tam & Hosoi 2011; Goldstein *et al.* 2016; Guo *et al.* 2021). In theoretical models for swimming flagella, their waveforms were typically prescribed as sinusoidal waves (Elfring *et al.* 2010; Cripe *et al.* 2016). In our models, flagellar waveforms are prescribed based on experimental observations, which is a more realistic representation but brings in some drawbacks, such as the exclusion of the phase-lag dependence of flagellar waveforms and the necessity for *a priori* information in flagellar beating.

The view prevails since Taylor (1951) that co-swimming sperm cells tend to form in-phase synchronisation to minimise the energy dissipation in the fluid. However, our results do not fully support this perspective. While in-phase synchronisation leads to relatively low power consumption, the minimum power can occur at a small flagellar phase lag due to the mechanical and hydrodynamic interactions (figure 5). Similarly, a recent computational study on two-dimensional co-swimming sheets has demonstrated that minimum power can occur at any flagellar phase lag, depending on the specific kinematics of the sheets (Liao & Lauga 2021). Moreover, a recent study on swimming paired flagella has indicated that the anti-phase synchronisation can induce the highest swimming speed and efficiency (Cripe *et al.* 2016), which is also found in our calculations. However, our simulations show that the highest swimming speed and efficiency of paired spermatozoa can result from flagellar phase lags besides π radians. To further confirm the existence of a statistical relationship between the swimming performances of paired spermatozoa and their flagellar beat patterns, a larger sample size is required.

Supplementary movie. A supplementary movie is available at https://doi.org/10.1017/jfm.2025.79.

Acknowledgements. K.Z. acknowledges financial support from the China Scholarship Council (CSC).

Funding. This work was supported by the European Research Council (ERC) under the European Union's Horizon 2020 Research and Innovation Programme under grant 866494 project-MAESTRO.

Declaration of interests. The authors declare no conflict of interest.

Author contributions. K.Z. and I.S.M.K. designed the research; K.Z. developed the models, analysed the data, and drafted the manuscript; A.L. and V.M. conducted the experiments; K.Z., A.K., V.M., S.M. and I.S.M.K. revised the manuscript.

Appendix A. Spatial discretisation of a sperm cell

In our models, the flagellum is discretised with cross-sections equally spaced along its length with a distance equal to its radius ρ. The cross-section is a circle. Six regularised Stokeslets are equally spaced along each circular cross-section, as illustrated in figure 8(*a*). The unit vectors $\boldsymbol{e}_1$ and $\boldsymbol{e}_2$ respectively align with the two principal axes of the ellipsoidal head, as illustrated in figure 1. Let $\boldsymbol{e}_3$ denote the unit vector aligned with the third principal axis of the ellipsoidal head, where $\boldsymbol{e}_3 = \boldsymbol{e}_1 \times \boldsymbol{e}_2$, as illustrated in figure 8(*b*). The sperm head is discretised with n_{h} cross-sections along its long axis (i.e. the axis aligned with vector $\boldsymbol{e}_1$). These n_{h} cross-sections are perpendicular to $\boldsymbol{e}_1$ and divide the elliptical cross-section of the ellipsoid at the $(\boldsymbol{e}_1, \boldsymbol{e}_3)$ plane into arcs. These arcs have the same arc length of approximate ρ by adjusting the distance between the n_{h} cross-sections. In each of the n_{h} cross-sections, regularised Stokeslets are equally spaced at distance approximately ρ. To discretise the walls, regularised Stokeslets are distributed on each wall in a square pattern with side length 10ρ, as illustrated in figure 8(*c*).

Appendix B. Calculation of hydrodynamic forces on paired sperm cells

For the total $n = n_1 + n_2 + n_{\mathrm{w}}$ regularised Stokeslets, the fluid response $\boldsymbol{u}$ at ${}^{m}\boldsymbol{r}$ to the hydrodynamic forces ${}^{k}\boldsymbol{f}$ is calculated by

$$\boldsymbol{u}({}^{m}\boldsymbol{r}) = -\frac{1}{8\pi\mu}\sum_{k=1}^{n}\sum_{p=1}^{3} S^{\epsilon}_{pq}({}^{k}\boldsymbol{r}, {}^{m}\boldsymbol{r})\,{}^{k}T\,{}^{k}_{p}\boldsymbol{f}, \quad m = 1, 2, \ldots, n, \tag{B1}$$

where ${}^{k}T$ is the quadrature weight of the kth regularised Stokeslets, ϵ is the regularisation parameter, and ${}^{k}_{p}\boldsymbol{f}$ is the pth component of the force on the cells by the fluid (Cortez *et al.* 2005).

Appendix C. Force balance and torque balance on each of the paired sperm cells

As the adhesive force and hydrodynamic forces on cell 1 are balanced, we have

$$\begin{aligned} \boldsymbol{C} &= \begin{bmatrix} {}^{1}\boldsymbol{C}_1 & {}^{2}\boldsymbol{C}_1 & \cdots & {}^{n_1}\boldsymbol{C}_1 & \boldsymbol{0}_{1\times 3(n_2+n_{\mathrm{w}})} \end{bmatrix}, & \boldsymbol{D} &= \begin{bmatrix} 0 & 0 & 0 & 0 & -1 & 0 \end{bmatrix}, \\ \boldsymbol{E} &= \begin{bmatrix} {}^{1}\boldsymbol{E}_1 & {}^{2}\boldsymbol{E}_1 & \cdots & {}^{n_1}\boldsymbol{E}_1 & \boldsymbol{0}_{1\times 3(n_2+n_{\mathrm{w}})} \end{bmatrix}, & \boldsymbol{F} &= \begin{bmatrix} 0 & 0 & 0 & 0 & 0 & -1 \end{bmatrix}, \end{aligned} \tag{C1}$$

where ${}^{k}\boldsymbol{C}_1 = [1\ 0\ 0]$ and ${}^{k}\boldsymbol{E}_1 = [0\ 1\ 0]$, $k = 1, 2, \ldots, n_1$. The torques due to these forces on cell 1 are balanced about the origin of the laboratory frame, so we have

$$\boldsymbol{G} = \begin{bmatrix} {}^{1}\boldsymbol{G}_1 & {}^{2}\boldsymbol{G}_1 & \cdots & {}^{n_1}\boldsymbol{G}_1 & \boldsymbol{0}_{1\times 3(n_2+n_{\mathrm{w}})} \end{bmatrix}, \quad \boldsymbol{H} = \begin{bmatrix} 0 & 0 & 0 & 0 & r_{\mathrm{p}y} & -r_{\mathrm{p}x} \end{bmatrix}, \tag{C2}$$

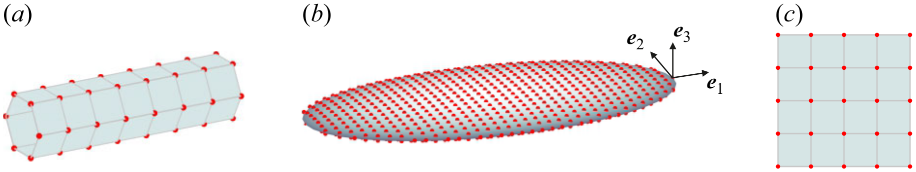

Figure 8. Spatial discretisation of the sperm (*a*) flagellum, (*b*) head and (*c*) wall. A portion of the flagellum and wall is shown.

where ${}^k\boldsymbol{G}_1 = [-{}^kr_{1y}\ {}^kr_{1x}\ 0]$, $k = 1, 2, \ldots, n_1$. Here, ${}^kr_{1x}$ and ${}^kr_{1y}$ are the components of the position vector of the kth point on cell 1 along the x- and y-axes of the laboratory frame, respectively. Likewise, r_{px} and r_{py} are the x- and y-components of $\boldsymbol{r}_\text{p}$. Based on the force balance on cell 2, we have

$$\left.\begin{aligned}\boldsymbol{I} &= \begin{bmatrix}\boldsymbol{0}_{1\times 3n_1} & {}^1\boldsymbol{I}_2 & {}^2\boldsymbol{I}_2 & \cdots & {}^{n_2}\boldsymbol{I}_2 & \boldsymbol{0}_{1\times 3n_\text{w}}\end{bmatrix}, & \boldsymbol{J} &= \begin{bmatrix}0 & 0 & 0 & 0 & 1 & 0\end{bmatrix},\\ \boldsymbol{K} &= \begin{bmatrix}\boldsymbol{0}_{1\times 3n_1} & {}^1\boldsymbol{K}_2 & {}^2\boldsymbol{K}_2 & \cdots & {}^{n_2}\boldsymbol{K}_2 & \boldsymbol{0}_{1\times 3n_\text{w}}\end{bmatrix}, & \boldsymbol{L} &= \begin{bmatrix}0 & 0 & 0 & 0 & 0 & 1\end{bmatrix},\end{aligned}\right\} \tag{C3}$$

where ${}^k\boldsymbol{I}_2 = [1\ 0\ 0]$ and ${}^k\boldsymbol{K}_2 = [0\ 1\ 0]$, $k = 1, 2, \ldots, n_2$. Based on the torque balance on cell 2 about the origin of the laboratory frame, we have

$$\boldsymbol{M} = \begin{bmatrix}\boldsymbol{0}_{1\times 3n_1} & {}^1\boldsymbol{M}_2 & {}^2\boldsymbol{M}_2 & \cdots & {}^{n_2}\boldsymbol{M}_2 & \boldsymbol{0}_{1\times 3n_\text{w}}\end{bmatrix}, \quad \boldsymbol{N} = \begin{bmatrix}0 & 0 & 0 & 0 & -r_{py} & r_{px}\end{bmatrix}, \tag{C4}$$

where ${}^k\boldsymbol{M}_2 = [-{}^kr_{2y}\ {}^kr_{2x}\ 0]$, $k = 1, 2, \ldots, n_2$. Here, ${}^kr_{2x}$ and ${}^kr_{2y}$ are the x- and y-components of the position vector of the kth point on cell 2, respectively.

Appendix D. Force balance and torque balance on a sperm pair

As the forces on a sperm pair are balanced, we have

$$\left.\begin{aligned}\boldsymbol{C}' &= \begin{bmatrix}{}^1\boldsymbol{C}'_1 & {}^2\boldsymbol{C}'_1 & \cdots & {}^{n_1}\boldsymbol{C}'_1 & {}^1\boldsymbol{C}'_2 & {}^2\boldsymbol{C}'_2 & \cdots & {}^{n_2}\boldsymbol{C}'_2 & \boldsymbol{0}_{1\times 3n_\text{w}}\end{bmatrix}, & \boldsymbol{D}' &= \boldsymbol{0}_{1\times 3},\\ \boldsymbol{E}' &= \begin{bmatrix}{}^1\boldsymbol{E}'_1 & {}^2\boldsymbol{E}'_1 & \cdots & {}^{n_1}\boldsymbol{E}'_1 & {}^1\boldsymbol{E}'_2 & {}^2\boldsymbol{E}'_2 & \cdots & {}^{n_2}\boldsymbol{E}'_2 & \boldsymbol{0}_{1\times 3n_\text{w}}\end{bmatrix}, & \boldsymbol{F}' &= \boldsymbol{0}_{1\times 3},\end{aligned}\right\} \tag{D1}$$

where ${}^k\boldsymbol{C}'_1 = [1\ 0\ 0]$ and ${}^k\boldsymbol{E}'_1 = [0\ 1\ 0]$, $k = 1, 2, \ldots, n_1$, with blocks ${}^k\boldsymbol{C}'_2 = [1\ 0\ 0]$ and ${}^k\boldsymbol{E}'_2 = [0\ 1\ 0]$, $k = 1, 2, \ldots, n_2$. The torques due to these forces on the sperm pair are balanced about the origin of the laboratory frame, so we have

$$\boldsymbol{G}' = \begin{bmatrix}{}^1\boldsymbol{G}'_1 & {}^2\boldsymbol{G}'_1 & \cdots & {}^{n_1}\boldsymbol{G}'_1 & {}^1\boldsymbol{G}'_2 & {}^2\boldsymbol{G}'_2 & \cdots & {}^{n_2}\boldsymbol{G}'_2 & \boldsymbol{0}_{1\times 3n_\text{w}}\end{bmatrix}, \quad \boldsymbol{H}' = \boldsymbol{0}_{1\times 3}, \tag{D2}$$

where ${}^k\boldsymbol{G}'_1 = [-{}^kr_{1y}\ {}^kr_{1x}\ 0]$, $k = 1, 2, \ldots, n_1$. Here, ${}^kr_{1x}$ and ${}^kr_{1y}$ are the components of the position vector of the kth point on cell 1 along the x- and y-axes of the laboratory frame, respectively, with blocks ${}^k\boldsymbol{G}'_2 = [-{}^kr_{2y}\ {}^kr_{2x}\ 0]$, $k = 1, 2, \ldots, n_2$, where ${}^kr_{2x}$ and ${}^kr_{2y}$ are the components of the position vector of the kth point on cell 2 along the x- and y-axes of the laboratory frame, respectively.

Appendix E. Verification of the spatial discretisation of spermatozoa

Following the approach of Cortez *et al.* (2005) and Gillies *et al.* (2009), we choose an optimal regularised parameter ϵ by comparing our predictions of the resistive force on two isolated ellipsoids translating in the x- and y-directions in an unbounded fluid with their exact solution. The first ellipsoid has the same dimensions as the sperm head

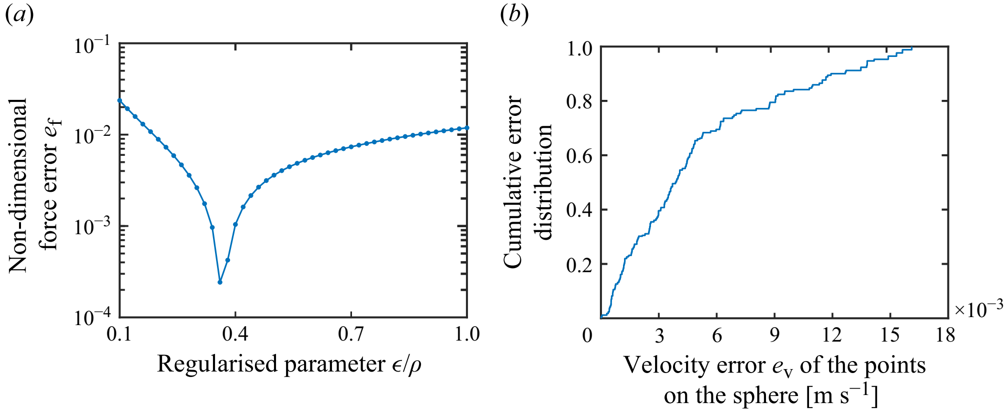

Figure 9. (*a*) Resistive force error e_f for two isolated ellipsoids is dependent on the regularised paratmeter ϵ. (*b*) Cumulative distribution of the velocity error e_v for the points on the sphere.

($9 \times 5 \times 0.4\,\mu$m), and is discretised using the same method as for the sperm head. The resistive force on a tube is often approximated using the slender body theory (Johnson 1980; Rodenborn *et al.* 2013). We represent the sperm flagellum with the second ellipsoid with an elongated needle-like geometry of $50 \times 0.25 \times 0.25\,\mu$m. is discretised using the same method as for the sperm flagellum. The non-dimensional resistive force error e_f is defined as

$$e_f = \sqrt{\frac{1}{n_c\,\zeta_{max}^2}\sum_{i=1}^{n_c}\zeta_i^2}, \tag{E1}$$

with $\zeta_i = \zeta_{exact} - \zeta_{pred}$, where ζ_{exact} is the exact resistive force on the ellipsoids (Kim 1986), and ζ_{pred} is our predicted resistive force on the ellipsoids. The number of the separate simulations is $n_c = 4$, i.e. the two ellipsoids translating in the x- and y-directions. Here, ζ_{max} is the maximum value of $\zeta_i,\ i = 1, 2, 3, 4$. The force error is minimised when $\epsilon = 0.36\rho$, as illustrated in figure 9(*a*). Using $\epsilon = 0.36\rho$, we further calculate the velocity U_z of the points on an isolated sphere moving with a unit velocity along the z-axis in an unbounded fluid. This sphere has a volume equivalent to that of the sperm head, and is discretised into 682 points in the same manner as for the sperm head. Cumulative distribution of velocity error for the points $e_v = |U_z - 1|$ shows that all the points have a velocity error less than 0.018 m s^{-1} (figure 9*b*). Note that the regularised parameter $\epsilon = 0.36\rho$ used here is to minimise the numerical error for the sperm head and flagellum moving in an unbounded fluid. Its value needs to be changed if walls are included.

Appendix F. Verification of the regularised parameter

In our test cases, $\xi = 0.5$ and $m = 0.9$ are chosen, which work well. Due to the lack of established convergence analysis for the regularised Stokeslets method (Ainley *et al.* 2008), we follow the approach of Ainley *et al.* (2008) and Gillies *et al.* (2009), and compare the predicted results in our test cases with published ones, as shown in figure 10. In our test cases, we calculate the resistive force $\boldsymbol{F}_s$ on a sphere translating in the x- and y-directions between the walls with velocity $\boldsymbol{U}_s$. This sphere has a volume equivalent to that of the sperm head. The walls are perpendicular to the z-axis. The resistive force $\boldsymbol{F}$ on the sphere translating in an unbounded fluid with the same velocity $\boldsymbol{U}_s$ is $\boldsymbol{F}_{s\infty} = 6\pi\mu r_s \boldsymbol{U}_s$, where μ is the viscosity of the fluid. The ratio $F_s/F_{s\infty}$ depends on the ratio h/r_s. As shown in

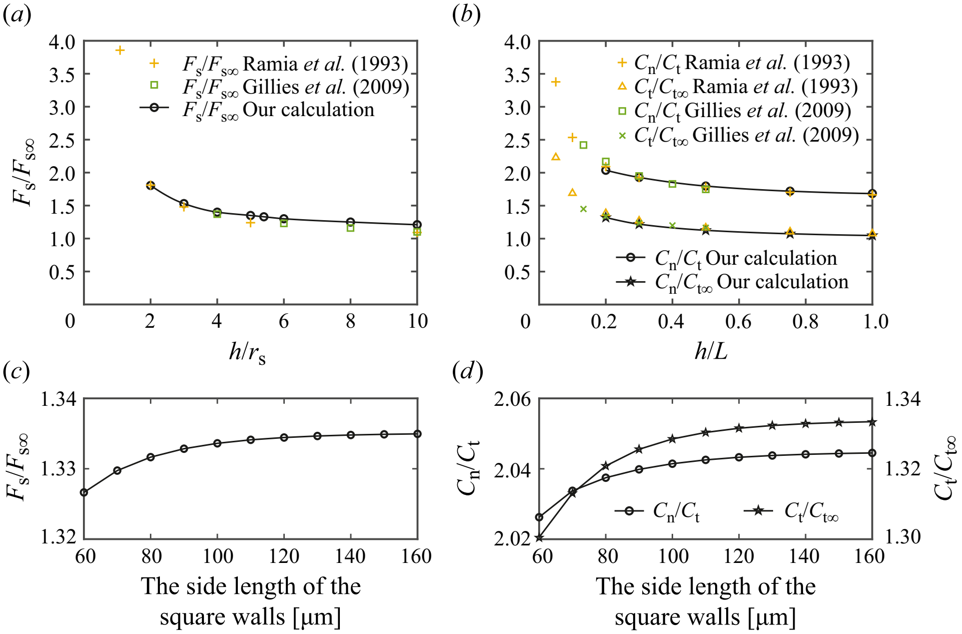

Figure 10. (*a*) Compared to the resistive force $F_{s\infty}$ on the sphere translating in an unbounded fluid, it experiences a larger resistive force F_s when translating between the walls with the same velocity. (*b*) For the isolated tube parallel to the walls, its normal resistance coefficient C_n is larger than its tangential resistance coefficient C_t. The tube translating in an unbounded fluid has a smaller tangential resistance coefficient $C_{t\infty}$ than that when translating between the walls. Our predictions for (*c*) $F_s/F_{s\infty}$ for the sphere, and (*d*) C_n/C_t and $C_t/C_{t\infty}$ for the tube are insensitive to the wall size.

figure 10(*a*), our theoretical results agree with those of Ramia *et al.* (1993) and Gillies *et al.* (2009).

In addition, we calculate the normal resistance coefficient C_n and tangential resistance coefficient C_t of an isolated tube translating in the radial and longitudinal directions between the walls. The tube is parallel to the walls. The tube has dimensions identical to those of the sperm flagellum, and is discretised in the same manner as for the flagellum. The ratios C_n/C_t and $C_t/C_{t\infty}$ depend on the ratio h/L, where $C_{t\infty}$ is the tangential resistance coefficient of an isolated tube translating in an unbounded fluid, as shown in figure 10(*b*). Our theoretical results agree with those of Ramia *et al.* (1993) and Gillies *et al.* (2009). Furthermore, as illustrated in figures 10(*c*,*d*), the wall size has only a slight impact on these ratios as long as the sphere and tube are covered by the walls. When the side length of the walls ranges from 60 to 160 μm, the maximum variation in $F_s/F_{s\infty}$ of the sphere is 0.6 %, and the maximum variations in C_n/C_t and $C_t/C_{t\infty}$ of the tube are 0.9 % and 2.5 %, respectively. Note that several different values of the wall half-depth h are included in our test cases, but $h = 10$ μm is kept fixed for all our further simulations, as the depth of the chamber that we used is 20 μm.

Appendix G. Reconstruction of flagellar shapes and their limit cycles

Using principal component analysis, we can approximate the tangent angle along each flagellum $\psi(l, t)$ as

$$\psi(l,t) \approx {}^0\psi(l) + \beta_1(t)\,\boldsymbol{V}_1(l) + \beta_2(t)\,\boldsymbol{V}_2(l), \tag{G1}$$

where ${}^0\psi(l)$ is the mean tangent angle (Geyer *et al.* 2013; Werner *et al.* 2014). Here, $\boldsymbol{V}_1$ and $\boldsymbol{V}_2$ are the first two flagellar shape modes, and β_1 and β_2 are their respective scores. This approximation accounts for 95 % of the variance of the tangent angles. To reduce the noise of the tangent angles, we approximated the flagellar shapes using smoothing splines before calculating the shape modes.

The flagellar shapes at different times were thereby mapped to the (β_1, β_2) space, represented by the points in the space (figure 4*b*). By fitting the points, we obtained the limit cycle. Flagellar phases were defined by binning flagellar shapes according to shape similarity. We then reconstructed flagellar tangent angles from the limit cycle. Finally, flagellar beat patterns with various phase lags were reconstructed from the tangent angles using (3.1).

Appendix H. Calculation of power consumption

After a sperm pair has established regular beating in our simulations, the instantaneous power dissipated in the fluid by the ith sperm cell at a time t_j is determined by

$$P_i\left(t_j\right)=\sum_{k=1}^{n_i}\left({}^k\boldsymbol{f}_i\left(t_j\right)\boldsymbol{\cdot}{}^k\boldsymbol{u}_i\left(t_j\right)\right), \tag{H1}$$

where n_i is the number of the regularised Stokeslets points on the ith sperm cell. The force ${}^k\boldsymbol{f}_i$ and the velocity ${}^k\boldsymbol{u}_i$ are determined from (4.6) or (4.9), depending on which model is used. The average power over one beat cycle for the ith cell is $\langle P_i\rangle=\sum_{j=1}^{n_\mathrm{t}} P_i(t_j)/n_\mathrm{t}$, where n_t is the number of time steps in this beat cycle. The average power per cell for the sperm pair is $\langle P\rangle=\sum_{i=1}^{2}\langle P_i\rangle/2$.

REFERENCES

AINLEY, J., DURKIN, S., EMBID, R., BOINDALA, P. & CORTEZ, R. 2008 The method of images for regularized Stokeslets. *J. Comput. Phys.* **227** (9), 4600–4616.

BAYLY, P., LEWIS, B., RANZ, E., OKAMOTO, R., PLESS, R. & DUTCHER, S. 2011 Propulsive forces on the flagellum during locomotion of *Chlamydomonas reinhardtii*. *Biophys. J.* **100** (11), 2716–2725.

BERG, H.C. & BROWN, D.A. 1972 Chemotaxis in *Escherichia coli* analysed by three-dimensional tracking. *Nature* **239** (5374), 500–504.

CARICHINO, L., DRUMM, D. & OLSON, S.D. 2021 A computational study of hydrodynamic interactions between pairs of sperm with planar and quasi-planar beat forms. *Front. Phys* **9**, 735438.

CARVALHO, J.O., SILVA, L.P., SARTORI, R. & DODE, M.A.N. 2013 Nanoscale differences in the shape and size of X and Y chromosome-bearing bovine sperm heads assessed by atomic force microscopy. *Plos One* **8** (3), 1–7.

CORTEZ, R., FAUCI, L. & MEDOVIKOV, A. 2005 The method of regularized stokeslets in three dimensions: analysis, validation, and application to helical swimming. *Phys. Fluids* **17** (3), 031504.

CRIPE, P., RICHFIELD, O. & SIMONS, J. 2016 Sperm pairing and measures of efficiency in planar swimming models. *Spora* **2** (1), 5.

DI LEONARDO, R., BÚZÁS, A., KELEMEN, L., VIZSNYICZAI, G., OROSZI, L. & ORMOS, P. 2012 Hydrodynamic synchronization of light driven microrotors. *Phys. Rev. Lett.* **109** (3), 034104.

DRESCHER, K., DUNKEL, J., CISNEROS, L.H., GANGULY, S. & GOLDSTEIN, R.E. 2011 Fluid dynamics and noise in bacterial cell–cell and cell–surface scattering. *Proc. Natl Acad. Sci.* **108** (27), 10940–10945.

EITER, T. & MANNILA, H. 1994 Computing discrete fréchet distance. *Tech Rep*. Technische Universitat Wien.

ELFRING, G.J. & LAUGA, E. 2009 Hydrodynamic phase locking of swimming microorganisms. *Phys. Rev. Lett.* **103** (8), 088101.

ELFRING, G.J. & LAUGA, E. 2011*a* Passive hydrodynamic synchronization of two-dimensional swimming cells. *Phys. Fluids* **23** (1), 011902.

ELFRING, G.J. & LAUGA, E. 2011*b* Synchronization of flexible sheets. *J. Fluid Mech.* **674**, 163–173.

ELFRING, G.J., PAK, O.S. & LAUGA, E. 2010 Two-dimensional flagellar synchronization in viscoelastic fluids. *J. Fluid Mech.* **646**, 505–515.

ELGETI, J., KAUPP, U. & GOMPPER, G. 2011 Response to comment on article: hydrodynamics of sperm cells near surfaces. *Biophys. J.* **100** (9), 2321–2324.

ELGETI, J., WINKLER, R.G. & GOMPPER, G. 2015 Physics of microswimmers – single particle motion and collective behavior: a review. *Rep. Prog. Phys.* **78** (5), 056601.

FISHER, H.S., GIOMI, L., HOEKSTRA, H.E. & MAHADEVAN, L. 2014 The dynamics of sperm cooperation in a competitive environment. *Proc. R. Soc. Lond. B: Biol. Sci.* **281** (1790), 20140296.

FISHER, H. & HOEKSTRA, H. 2010 Competition drives cooperation among closely related sperm of deer mice. *Nature* **463** (7282), 801–803.

FLAHERTY, S.P., SWANN, N.J., PRIMAKOFF, P. & MYLES, D.G. 1993 A role for the WH-30 protein in sperm–sperm adhesion during rouleaux formation in the guinea pig. *Dev. Biol.* **156** (1), 243–252.

FRIEDRICH, B.M. & JÜLICHER, F. 2007 Chemotaxis of sperm cells. *Proc. Natl Acad. Sci.* **104** (33), 13256–13261.

FRIEDRICH, B.M., RIEDEL-KRUSE, I.H., HOWARD, J. & JÜLICHER, F. 2010 High-precision tracking of sperm swimming fine structure provides strong test of resistive force theory. *J. Exp. Biol.* **213** (8), 1226–1234.

GEYER, V.F., JÜLICHER, F., HOWARD, J. & FRIEDRICH, B.M. 2013 Cell-body rocking is a dominant mechanism for flagellar synchronization in a swimming alga. *Proc. Natl Acad. Sci.* **110** (45), 18058–18063.

GILLIES, E.A., CANNON, R.M., GREEN, R.B. & PACEY, A.A. 2009 Hydrodynamic propulsion of human sperm. *J. Fluid Mech.* **625**, 445–474.

GOLDSTEIN, R.E., LAUGA, E., PESCI, A.I. & PROCTOR, M.R.E. 2016 Elastohydrodynamic synchronization of adjacent beating flagella. *Phys. Rev. Fluids* **1** (7), 073201.

GOLESTANIAN, R., YEOMANS, J.M. & UCHIDA, N. 2011 Hydrodynamic synchronization at low Reynolds number. *Soft Matter* **7** (7), 3074–3082.

GONG, A., RODE, S., KAUPP, U.B., GOMPPER, G., ELGETI, J., FRIEDRICH, B.M. & ALVAREZ, L. 2020 The steering gaits of sperm. *Phil. Trans. R. Soc. Lond. B: Biol. Sci.* **375** (1792), 20190149.

GUO, H., FAUCI, L., SHELLEY, M. & KANSO, E. 2018 Bistability in the synchronization of actuated microfilaments. *J. Fluid Mech.* **836**, 304–323.

GUO, H., MAN, Y., WAN, K.Y. & KANSO, E. 2021 Intracellular coupling modulates biflagellar synchrony. *J. R. Soc. Interface* **18** (174), 20200660.

HICKEY, D.J., GOLESTANIAN, R. & VILFAN, A. 2023 Nonreciprocal interactions give rise to fast cilium synchronization in finite systems. *Proc. Natl Acad. Sci.* **120** (40), e2307279120.

IMMLER, S. 2008 Sperm competition and sperm cooperation: the potential role of diploid and haploid expression. *Reproduction* **135** (3), 275–283.

ISHIKAWA, T. & HOTA, M. 2006 Interaction of two swimming *Paramecia*. *J. Exp. Biol.* **209** (22), 4452–4463.

JOHNSON, R.E. 1980 An improved slender-body theory for Stokes flow. *J. Fluid Mech.* **99** (2), 411–431.

KIM, S. 1986 Singularity solutions for ellipsoids in low-Reynolds-number flows: with applications to the calculation of hydrodynamic interactions in suspensions of ellipsoids. *Intl J. Multiphase Flow* **12** (3), 469–491.

KLINDT, G.S., RULOFF, C., WAGNER, C. & FRIEDRICH, B.M. 2017 In-phase and anti-phase flagellar synchronization by waveform compliance and basal coupling. *New J. Phys.* **19** (11), 113052.

LAUGA, E. & POWERS, T.R. 2009 The hydrodynamics of swimming microorganisms. *Rep. Prog. Phys.* **72** (9), 096601.

LEPTOS, K.C., WAN, K.Y., POLIN, M., TUVAL, I., PESCI, A.I. & GOLDSTEIN, R.E. 2013 Antiphase synchronization in a flagellar-dominance mutant of *Chlamydomonas*. *Phys. Rev. Lett.* **111** (15), 158101.

LI, C., CHAKRABARTI, B., CASTILLA, P., MAHAJAN, A. & SAINTILLAN, D. 2023 Chemomechanical model of sperm locomotion reveals two modes of swimming. *Phys. Rev. Fluids* **8** (11), 113102.

LIAO, W. & LAUGA, E. 2021 Energetics of synchronization for model flagella and cilia. *Phys. Rev. E* **103** (4), 042419.

LINDAHL, P.E. & SJÖBLOM, P. 1981 On mechanisms of head-to-head association in bovine spermatozoa. *Biol. Reprod.* **25** (1), 29–43.

MA, R., KLINDT, G.S., RIEDEL-KRUSE, I.H., JÜLICHER, F. & FRIEDRICH, B.M. 2014 Active phase and amplitude fluctuations of flagellar beating. *Phys. Rev. Lett.* **113** (4), 048101.

MACHEMER, H. & ECKERT, R. 1973 Electrophysiological control of reversed ciliary beating in *Paramecium*. *J. Gen. Physiol.* **61** (5), 572–587.

MOORE, H., KOMRSKOVA, K., JENKINS, N. & BREED, W. 2002 Exceptional sperm cooperation in the wood mouse. *Nature* **418** (6894), 174–177.

MORCILLO I SOLER, P., HIDALGO, C., FEKETE, Z., ZALANYI, L., KHALIL, I., YESTE, M. & MAGDANZ, V. 2022 Bundle formation of sperm: influence of environmental factors. *Front. Endocrinol.* **13**, 957684.

NAWROTH, J., VAN DER DOES, A., FIRTH, A.M., KANSO, E. 2019 Multiscale mechanics of mucociliary clearance in the lung. *Phil. Trans. R. Soc. B: Biol. Sci.* **375** (1792), 20190160.

OKAMOTO, K.I. & NAKAOKA, Y. 1994 Reconstitution of metachronal waves in ciliated cortical sheets of *Paramecium*: I. Wave stabilities. *J. Expl Biol.* **192** (1), 61–72.

OLSON, S.D. & FAUCI, L.J. 2015 Hydrodynamic interactions of sheets vs filaments: synchronization, attraction, and alignment. *Phys. Fluids* **27** (12), 121901.

OLSTAD, E., RINGERS, C., HANSEN, J., WENS, A., BRANDT, C., WACHTEN, D., YAKSI, E. & JURISCH-YAKSI, N. 2019 Ciliary beating compartmentalizes cerebrospinal fluid flow in the brain and regulates ventricular development. *Curr. Biol.* **29** (2), 229–241.

OMORI, T., ITO, H. & ISHIKAWA, T. 2020 Swimming microorganisms acquire optimal efficiency with multiple cilia. *Proc.Natl Acad. Sci.* **117** (48), 30201–30207.

OSTERMAN, N. & VILFAN, A. 2011 Finding the ciliary beating pattern with optimal efficiency. *Proc. Natl Acad. Sci.* **108** (38), 15727–15732.

PEARCE, D.J.G., HOOGERBRUGGE, L.A., HOOK, K.A., FISHER, H.S. & GIOMI, L. 2018 Cellular geometry controls the efficiency of motile sperm aggregates. *J. R. Soc. Interface* **15** (148), 20180702.

PESCH, S. & BERGMANN, M. 2006 Structure of mammalian spermatozoa in respect to viability, fertility and cryopreservation. *Micron* **37** (7), 597–612.

POLIN, M., TUVAL, I., DRESCHER, K., GOLLUB, J.P. & GOLDSTEIN, R.E. 2009 *Chlamydomonas* swims with two gears in a eukaryotic version of run-and-tumble locomotion. *Science* **325** (5939), 487–490.

POOLEY, C.M., ALEXANDER, G.P. & YEOMANS, J.M. 2007 Hydrodynamic interaction between two swimmers at low Reynolds number. *Phys. Rev. Lett.* **99** (22), 228103.

PRAMANIK, R., VERSTAPPEN, R.W.C.P. & ONCK, P.R. 2024 Nature-inspired miniaturized magnetic soft robotic swimmers. *Appl. Phys. Rev.* **11** (2), 021312.

QUARANTA, G., AUBIN-TAM, M.E. & TAM, D. 2015 Hydrodynamics versus intracellular coupling in the synchronization of eukaryotic flagella. *Phys. Rev. Lett.* **115** (23), 238101.

RAMIA, M., TULLOCK, D. & PHAN-THIEN, N. 1993 The role of hydrodynamic interaction in the locomotion of microorganisms. *Biophys. J.* **65** (2), 755–778.

RAVESHI, M., ABDUL HALIM, M.S., AGNIHOTRI, S., O'BRYAN, M., NEILD, A. & NOSRATI, R. 2021 Curvature in the reproductive tract alters sperm–surface interactions. *Nat. Commun.* **12** (1), 3446.

RIEDEL-KRUSE, I., HILFINGER, A., HOWARD, J. & JÜLICHER, F. 2007 How molecular motors shape the flagellar beat. *HFSP J.* **1** (3), 192–208.

RODENBORN, B., CHEN, C.H., SWINNEY, H.L., LIU, B. & ZHANG, H.P. 2013 Propulsion of microorganisms by a helical flagellum. *Proc. Natl Acad. Sci.* **110** (5), E338–E347.

SAMATAS, S. & LINTUVUORI, J. 2023 Hydrodynamic synchronization of chiral microswimmers. *Phys. Rev. Lett.* **130** (2), 024001.

SIMONS, J., FAUCI, L. & CORTEZ, R. 2015 A fully three-dimensional model of the interaction of driven elastic filaments in a Stokes flow with applications to sperm motility. *Journal of Biomechanics*, **48** (9) pp. 1639–1651.

SIMONS, J. & ROSENBERGER, A. 2021 Flagellar cooperativity and collective motion in sperm. *Fluids* **6** (10), 353.

SMITH, D.J., GAFFNEY, E.A., BLAKE, J.R. & KIRKMAN-BROWN, J.C. 2009 Human sperm accumulation near surfaces: a simulation study. *J. Fluid Mech.* **621**, 289–320.

TAKETOSHI, N., OMORI, T. & ISHIKAWA, T. 2020 Elasto-hydrodynamic interaction of two swimming spermatozoa. *Phys. Fluids* **32** (10), 101901.

TAM, D. & HOSOI, A.E. 2011 Optimal feeding and swimming gaits of biflagellated organisms. *Proc. Natl Acad. Sci.* **108** (3), 1001–1006.

TĂTULEA-CODREAN, M. & LAUGA, E. 2022 Elastohydrodynamic synchronization of rotating bacterial flagella. *Phys. Rev. Lett.* **128** (20), 208101.

TAYLOR, G.I. 1951 Analysis of the swimming of microscopic organisms. *Proc. R. Soc. Lond. A: Math. Phys. Sci.* **209**, 447–461.

TU, H.Q. *et al.*et al. 2023 Rhythmic cilia changes support SCN neuron coherence in circadian clock. *Science* **380** (6648), 972–979.

TUNG, C.K., LIN, C., HARVEY, B., FIORE, A., ARDÓN, F., WU, M. & SUAREZ, S. 2017 Fluid viscoelasticity promotes collective swimming of sperm. *Sci. Rep.* **7** (1), 3152.

UCHIDA, N. & GOLESTANIAN, R. 2011 Generic conditions for hydrodynamic synchronization. *Phys. Rev. Lett.* **106** (5), 058104.

WAN, K.Y. & GOLDSTEIN, R.E. 2016 Coordinated beating of algal flagella is mediated by basal coupling. *Proc. Natl Acad. Sci.* **113** (20), E2784–E2793.

WAN, K.Y., LEPTOS, K.C. & GOLDSTEIN, R.E. 2014 Lag, lock, sync, slip: the many ‘phases’ of coupled flagella. *J. R. Soc. Interface* **11** (94), 20131160.

WERNER, S., RINK, J.C., RIEDEL-KRUSE, I.H. & FRIEDRICH, B.M. 2014 Shape mode analysis exposes movement patterns in biology: flagella and flatworms as case studies. *PLOS One* **9** (11), 1–21.

WINET, H., BERNSTEIN, G.S. & HEAD, J. 1984 Observations on the response of human spermatozoa to gravity, boundaries and fluid shear. *Reproduction* **70** (2), 511–523.

WOOLLEY, D.M. 2003 Motility of spermatozoa at surfaces. *Reproduction* **126** (2), 259–270.

WOOLLEY, D.M., CROCKETT, R.F., GROOM, W.D.I. & REVELL, S.G. 2009 A study of synchronisation between the flagella of bull spermatozoa, with related observations. *J. Exp. Biol.* **212** (14), 2215–2223.

YANG, Y., ELGETI, J. & GOMPPER, G. 2008 Cooperation of sperm in two dimensions: synchronization, attraction, and aggregation through hydrodynamic interactions. *Phys. Rev. E* **78** (6), 061903.

YUNDT, A., SHACK, W. & LARDNER, T. 1975 Applicability of hydrodynamic analyses of spermatozoan motion. *J. Exp. Biol.* **62** (1), 27–41.

ZAFERANI, M. & ABBASPOURRAD, A. 2023 Biphasic chemokinesis of mammalian sperm. *Phys. Rev. Lett.* **130** (24), 248401.

ZAFERANI, M., JAVI, F., MOKHTARE, A., LI, P. & ABBASPOURRAD, A. 2021 Rolling controls sperm navigation in response to the dynamic rheological properties of the environment. *eLife* **10**, e68693.

ZHANG, K., KLINGNER, A., LE GARS, Y., MISRA, S., MAGDANZ, V. & KHALIL, I.S.M. 2023 Locomotion of bovine spermatozoa during the transition from individual cells to bundles. *Proc. Natl Acad. Sci.* **120** (3), e2211911120.